國立交通大學

電機學院微電子奈米科技產業研發碩士班

碩士論文

電子束微影技術的鄰近效應研究

A study of proximity effect in E-beam lithography

研究生： 方禎祥

指導教授： 黃遠東 教授

林俊宏 博士

中華民國九十六年八月

電子束微影技術的鄰近效應研究

A study of proximity effect in E-beam lithography

研 究 生: 方禎祥　　Student ： Chen-Hsiang Fang

指導教授： 黃遠東　　Advisor： Yang-Tung Huang

林俊宏　　Chun-Hung Lin

國 立 交 通 大 學

電機學院微電子奈米科技產業研發碩士班

碩 士 論 文

A Thesis

Submitted to College of Electrical and Computer Engineering

National Chiao Tung University

in partial Fulfillment of the Requirements

for the Degree of

Master

in

Industrial Technology R & D Master Program on
Microelectronics and Nano Sciences

August 2007

Hsinchu, Taiwan, Republic of China

中華民國九十六年八月

電子束微影技術的鄰近效應研究

學生：方禎祥　　　　指導教授：黃遠東
林俊宏

國立交通大學電機學院產業研發碩士班

摘　　要

本論文研製之電子束微影技術的鄰近效應研究,包含鄰近效應參數及鄰近效應修正。我們開發一個以蒙地卡羅為基礎的模擬程式,用來計算鄰近效應參數,另外從我們所設計的圖案,鄰近效應參數也可由實驗量測資料以雙高斯函數模型粹取出來。以這些鄰近效應參數及設計圖案,我們使用一鄰近效應修正軟體,PROXECCO,來產出鄰近效應修正圖案檔。之後從實驗量測數據,我們展示出重大的鄰近效應修正成果。我們使用可變形狀電子束曝光系統「Leica WePrint 200」,可以成功曝出小於100奈米的奈米級的圖案。

A study of proximity effect in E-beam lithography

student: Chen-Hsiang Fang　　　　　Advisors： Dr. Yang-Tung Huang
Dr. Chun-Hung Lin

Industrial Technology R & D Master Program of
Electrical and Computer Engineering College
National Chiao Tung University

ABSTRACT

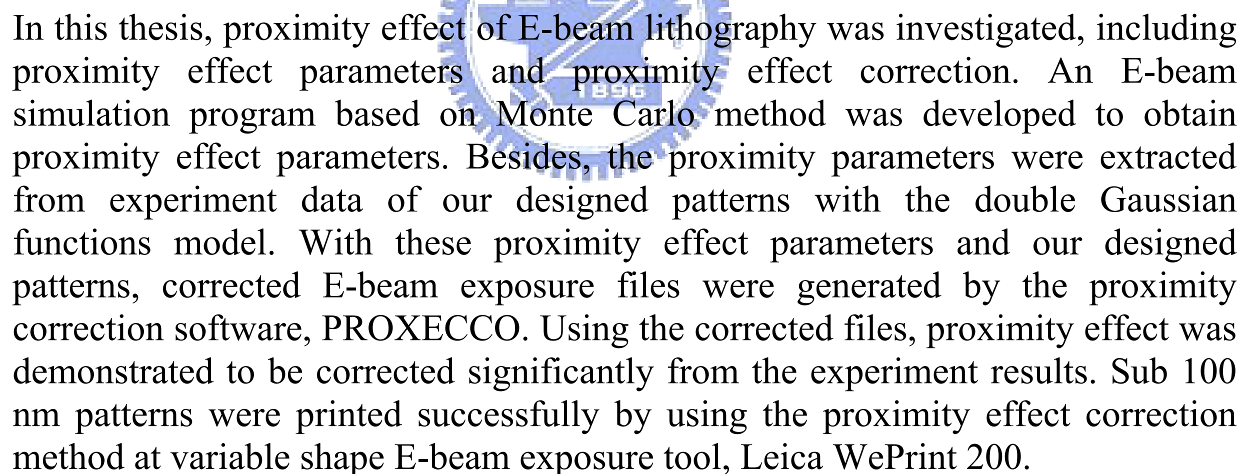

In this thesis, proximity effect of E-beam lithography was investigated, including proximity effect parameters and proximity effect correction. An E-beam simulation program based on Monte Carlo method was developed to obtain proximity effect parameters. Besides, the proximity parameters were extracted from experiment data of our designed patterns with the double Gaussian functions model. With these proximity effect parameters and our designed patterns, corrected E-beam exposure files were generated by the proximity correction software, PROXECCO. Using the corrected files, proximity effect was demonstrated to be corrected significantly from the experiment results. Sub 100 nm patterns were printed successfully by using the proximity effect correction method at variable shape E-beam exposure tool, Leica WePrint 200.

Acknowledgement

I want to express my gratitude to my advisors, Dr. Yang-Tung Huang and Dr. Chun-Hung Lin, for their support and guidance on my research. Dr. Cheng-May Kwei also taught me a lot in her lecture. Their ideas and advices helped me to correct many errors.

Then, I want to thank all the members of Nanophotonics & Biophotonics Laboratory and all the persons in National Nano Device Laboratory. They helped me a lot to finish the work and experiments of the research.

Finally, I would give my greatest appreciation to my family for their assistance and love.

This work was supported by the National Science Council of the Republic of China under contract NSC 95-2221-E-492-015.

Contents

CHAPTER 1. INTRODUCTION **1**

CHAPTER 2. ELECTRON INTERACTION OF E-BEAM LITHOGRAPHY **4**

2.1. ELECTRON SCATTERING PROCESSES 4

2.2. PROXIMITY EFFECT 5

2.3. PROXIMITY EFFECT CORRECTION 7

2.3.1. Proximity effect parameters *7*

2.3.1.1. Doughnut Type 7

2.3.1.2. Point Type 8

2.3.1.3. SCELETON 9

2.4. PROXIMITY EFFECT CORRECTION METHODS 9

2.4.1. Dose correction *9*

2.4.2. Shape compensation *10*

2.4.3. Background correction *11*

2.4.4. Top surface image method *12*

CHAPTER 3. MONTE CARLO SIMULATION FOR E-BEAM LITHOGRAPHY **14**

3.1. MONTE CARLO MODELS 14

3.1.1. Multiple scattering model *14*

3.1.2. Single scattering model *14*

3.1.3. Hybrid model *15*

3.1.4. Direct simulation model *15*

3.1.5. Dielectric function model *15*

3.2. ELECTRON INTERACTION WITH ATOM 15

3.2.1. Elastic collision *15*

3.2.2. Inelastic collision *18*

3.3. PC SIMULATION 18

3.3.1. Density calculation *18*

3.3.2. Components analysis *19*

3.3.3. Mean free path random number R1 .... *20*

3.3.4. Scattering center atom random number R2 .... *21*

3.3.5. Angle of scattering random number R3 .... *21*

3.3.6. Azimuthal angle random number R4 .... *21*

3.3.7. Trajectory of scattering *22*

3.4. VERIFICATION 22

3.4.1. Stopping power *23*

3.4.2. *Penetration and reflection ratio* 24
3.4.3. *Energy profile* 25
3.5. SIMULATION RESULT 27
3.5.1. *Electron transverse path* 27
3.5.2. *Energy parameter fitting* 28
3.6. PROXIMITY EFFECT PARAMETERS OF MONTE CARLO METHOD 28
CHAPTER 4. EXPERIMENT AND DISCUSSION 30
4.1. EXPERIMENT PROCESS 30
4.1.1. *Experiment equipments* 30
4.1.2. *Experiment process* 30
4.1.3. *Clean Track coating* 31
4.1.4. *E-beam exposure* 32
4.1.5. *Clean Track developing* 33
4.1.6. *CD measurement* 33
4.2. TEST PATTERNS 33
4.3. FITTING ALGORITHM 34
4.4. FILM STRUCTURE 35
4.5. EXPERIMENT RESULT 36
4.5.1. *Proximity effect parameters of Exp-Ext-W2 method* 36
4.5.2. *Proximity effect parameters of Exp-Fit-W10 method* 37
4.5.3. *Proximity effect parameters comparison of different method* 38
4.5.4. *Proximity correction result of Si substrate* 39
4.5.5. *Proximity correction result of Nitride film* 43
4.5.6. *Proximity correction result of Wet-Oxide film* 47
4.5.7. *Proximity correction result of Ta film* 51
4.5.8. *Proximity correction result of Copper film* 55
4.6. DISCUSSION 59
CHAPTER 5. CONCLUSION AND FUTURE WORK 62
REFERENCE 63

List of tables

Table 3-1 atomic percentage of NEB-A4 photo-resist film derived from ESCA 20
Table 3-2 Atomic weight percentage of elements in photoresist NEB-A4 obtained from EA 20
Table 3-3 Verification of stopping range of different accelerated voltage of PMMA and silicon 23
Table 3-4 Comparison of penetration ratio of 400 nm PMMA on silicon substrate of different acceleration voltage 20KV, 10KV, 5KV. 24
Table 3-5 Comparison of reflection ratio of 400 nm PMMA on silicon substrate of different acceleration voltage 20KV, 10KV, 5KV. 25
Table 3-6 Test result of our developed Monte Carlo method for different film structures. 29
Table 4-1 Proximity effect parameters extracted from the measurement data with Exp-Ext-W2 weightings..........37
Table 4-2 Proximity effect parameters extracted from the measurement data with Exp-Ext-W10 weightings........37

List of Figures

Fig 1-1 Potential lithography solution for next generation lithography from ITRS, Y2005 version [2]. 2

Fig 1-2 E-beam lithography evolution [9]....3

Fig 2-1 Electrons trajectories schema to show electron scattering path of E-beam lithography. 5

Fig 2-2 Test patterns for proximity effect and simulation result (a)Designed test patterns for checking proximity effect (b) Simulated result of uncorrected proximity effect exposure [14]. .6

Fig 2-3 Test cell of the Doughnut-method [15]. R1 is variable while R2 is fixed and much larger than backward scattering range....8

Fig 2-4 Normalized exposure on silicon at 25 KeV by point exposure method [12]. 9

Fig 2-5 (a) Pattern corrected by PROXECCO with coarse resolution. (b)Simulation exposed result of PROXECCO with coarse resolution correction [14]. 10

Fig 2-6 Graphical illustration of IMR (inner maximum rectangular) adjustment and shape correction at corner and its simulated correction effect [22]. The left part is the modified exposure pattern, the right part is the simulation result of deposited energy 11

Fig 2-7 Energy distribution of combination of pattern exposure and correction exposure [21].......12

Fig 2-8 A bi-layer process using top surface image of low energy E-beam lithography to alleviate proximity effect [33]. 13

Fig 3-1 ESCA spectrum for NEB-A4 photo-resist film. The elements for the analysis are C,O,N and S. 19

Fig 3-2 One step of electron movement in 2D schematic drawing. 22

Fig 3-3 Constant energy density contour of 0.5 μm line for mask case. The source is Gaussian beam with 50nm range, at 20 KeV [30]....26

Fig 3-4 Simulation energy density contour of 0.5 μm line of our developed program. The source is Gaussian beam of range 50nm at 20KeV. 26

Fig 3-5 simulated electron path for 400 nm NEB film on Silicon substrate with 40KeV electron beam. 27

Fig 3-6 Gaussian fitting of backscattered energy of 40KV E-beam Exposure for 400nm NEB on 1000nm copper with silicon substrate....28

Fig 4-1 wafer process flow for proximity effect extraction with uncorrected design patterns. 31

Fig 4-2 wafer process flow for proximity effect correction check with proximity effect correction patterns....31

Fig 4-3 schematic drawing of beam path of Leica WePint 200 [31]. 32

Fig 4-4 schematic drawing of designed patterns to extract proximity effect parameters and to check proximity effect correction result....34

Fig 4-5 Comparison chart of backscattering energy to forward scattering energy ratio for 5 types of substrates....38

Fig 4-6 Comparison chart of backscattered range for 5 types of substrates....39

Fig 4-7 ADI CD comparison of silicon trench for proximity effect correction parameters from empirical and Monte Carlo methods. 40
Fig 4-8 ADI CD comparison of silicon Isolated lines for proximity effect correction parameters from empirical and Monte Carlo methods. 40
Fig 4-9 ADI CD comparison of silicon dense lines for proximity effect correction parameters from empirical and Monte Carlo methods. 41
Fig 4-10 ADI CD comparison of silicon dense dots for proximity effect correction parameters from empirical and Monte Carlo methods. 41
Fig 4-11 ADI CD comparison of silicon isolated dots for proximity effect correction parameters from empirical and Monte Carlo methods. 42
Fig 4-12 Proximity correction result of 80 nm silicon isolated line with Exp-Ext-W2 method. The design CD is 80nm. The measured CD is 79nm. 42
Fig 4-13 Proximity correction result of 80 nm silicon isolated line with Monte Carlo method. The design CD is 80nm. The measured CD is 70nm. 43
Fig 4-14 Proximity correction result of 80 nm silicon isolated line with Exp-Ext-W10 method. The design CD is 80nm. The measured CD is 76nm. 43
Fig 4-15 ADI CD comparison of nitride trench for proximity effect correction parameters from empirical and Monte Carlo methods. 44
Fig 4-16 ADI CD comparison of nitride isolated lines for proximity effect correction parameters from empirical and Monte Carlo methods. 44
Fig 4-17 ADI CD comparison of nitride dense lines for proximity effect correction parameters from empirical and Monte Carlo methods. 45
Fig 4-18 ADI CD comparison of nitride dense dots for proximity effect correction parameters from empirical and Monte Carlo methods. 45
Fig 4-19 Nitride Isolated Dot ADI CD comparison for proximity effect correction parameters from empirical and Monte Carlo methods. 46
Fig 4-20 Proximity correction result of 80 nm nitride isolated line with Exp-Ext-W2 method. The design CD is 80nm. The measured CD is 80nm. 46
Fig 4-21 Proximity correction result of 80 nm nitride isolated line with Monte Carlo method. The design CD is 80nm. The measured CD is 72nm. 47
Fig 4-22 Proximity correction result of 80 nm nitride isolated line with Exp-Ext-W10 method. The design CD is 80nm. The measured CD is 81nm. 47
Fig 4-23 ADI CD comparison of wet oxide trench for proximity effect correction parameters from empirical and Monte Carlo methods. 48
Fig 4-24 ADI CD comparison of wet oxide isolated lines for proximity effect correction parameters from empirical and Monte Carlo methods. 48
Fig 4-25 ADI CD comparison of wet oxide dense lines for proximity effect correction parameters from empirical and Monte Carlo methods. 49

Fig 4-26 ADI CD comparison of wet oxide dense dots for proximity effect correction parameters from empirical and Monte Carlo methods. 49
Fig 4-27 Wet Oxide Isolated Dot ADI CD comparison for proximity effect correction parameters from empirical and Monte Carlo methods. 50
Fig 4-28 Proximity correction result of 80 nm wet oxide isolated line with Exp-Ext-W2 method. The design CD is 80nm. The measured CD is 76nm. 50
Fig 4-29 Proximity correction result of 80 nm wet oxide isolated line with Monte Carlo method. The design CD is 80nm. The measured CD is 73nm. 51
Fig 4-30 Proximity correction result of 80 nm wet oxide isolated line with Exp-Ext-W10 method. The design CD is 80nm. The measured CD is 75nm. 51
Fig 4-31 ADI CD comparison of Ta trench for proximity effect correction parameters from empirical and Monte Carlo methods. 52
Fig 4-32 ADI CD comparison of Ta isolated lines for proximity effect correction parameters from empirical and Monte Carlo methods. 52
Fig 4-33 ADI CD comparison of Ta dense lines for proximity effect correction parameters from empirical and Monte Carlo methods. 53
Fig 4-34 ADI CD comparison of Ta dense dots for proximity effect correction parameters from empirical and Monte Carlo methods. 53
Fig 4-35 ADI CD comparison of Ta isolated dots for proximity effect correction parameters from empirical and Monte Carlo methods. 54
Fig 4-36 Proximity correction result of 80 nm Ta isolated line with Exp-Ext-W2 method. The design CD is 80nm. The measured CD is 57nm. 54
Fig 4-37 Proximity correction result of 80 nm Ta isolated line with Monte Carlo method. The design CD is 80nm. The measured CD is 73nm. 55
Fig 4-38 Proximity correction result of 80 nm Ta isolated line with Exp-Ext-W10 method. The design CD is 80nm. The measured CD is 61nm. 55
Fig 4-39 ADI CD comparison of copper trench for proximity effect correction parameters from empirical and Monte Carlo methods. 56
Fig 4-40 ADI CD comparison of copper isolated lines for proximity effect correction parameters from empirical and Monte Carlo methods. 56
Fig 4-41 ADI CD comparison of copper dense lines for proximity effect correction parameters from empirical and Monte Carlo methods. 57
Fig 4-42 ADI CD comparison of copper dense dots for proximity effect correction parameters from empirical and Monte Carlo methods. 57
Fig 4-43 ADI CD comparison of copper isolated dots for proximity effect correction parameters from empirical and Monte Carlo methods. 58
Fig 4-44 Proximity correction result of 200 nm Cu isolated line with Exp-Ext-W2 method. The design CD is 200nm. The measured CD is 198nm. 58

Fig 4-45 Proximity correction result of 280 nm Cu isolated line with Monte Carlo method. The design CD is 280nm. The measured CD is 277nm. 59
Fig 4-46 Proximity correction result of 200 nm Cu isolated line with Exp-Ext-W10 method. The design CD is 200nm. The measured CD is 203nm. 59
Fig 4-47 PR lifting of isolated line of 260 nm on copper film. 60
Fig 4-48 cross link density chart of 100 nm isolated line of NEB-A4 photoresist. 61

Chapter 1.

Introduction

Lithography plays an important role in the manufacturing of ICs. In the early days, contact printing tools were used. The cross contamination between masks and wafers kills the chip yield of the wafers. The proximity printing tools were introduced to reduce the cross contamination. Poor resolution limits the wide application of the systems. Projection system was introduced to overcome above issues. The continuous improving of projection tools minimized the line width of ICs and made semiconductor industry follow the pace of Moore's law.

The resolution of optical projection lithography follows the Rayleigh's criterion. The equation of Rayleigh's criterion is

$$R = k_1 \frac{\lambda}{NA} \tag{1.1}$$

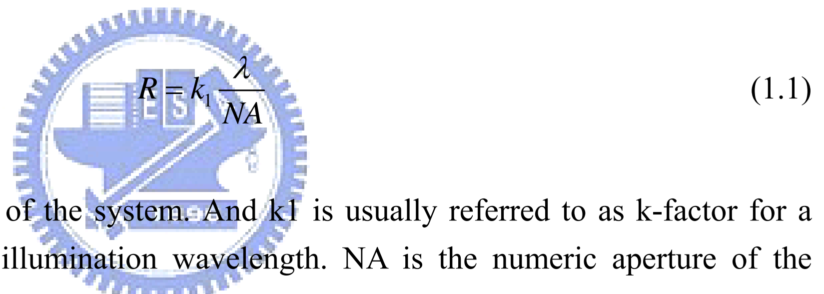

where R is the resolution limit of the system. And k1 is usually referred to as k-factor for a given photo process, λ is the illumination wavelength. NA is the numeric aperture of the projection system. The improvement of projection systems includes enlargement of NA, shortening of illumination wavelength, reduction of process factor. NA of stepper has increased from 0.28, the NA of first stepper from GCA, to about 1.3, the NA of water immersion scanner. Illumination wavelength was shortened from 436 nm, g-line of mercury lamp, to 193 nm, characteristic wavelength of ArF excimer laser. K1 was reduced from 0.7 to 0.3 through the improvement of photoresist characteristics and the use of RET (resolution enhancement technology). But the resolution faces the practical physical restriction of current developed material for future technology node. For example, lens material damage at 126 nm wavelength is a particular problem. And there are other issues that will more likely prevent the extension of optical lithography to wavelength smaller than 157 nm. Optical lithography will face resolution limit to about 30 nm [1].

What will be the dominant lithography technology after optical lithography? From the roadmap of ITRS (International Technology Roadmap for semiconductor) [2], ML2 (mask-less lithography), EUVL (Extreme ultraviolet lithography) and NIL (nanometer imprint lithography) will be the candidates for next generation lithography (NGL). EUVL uses 13 nm illumination wavelength with all reflection lens system. The stability of the illumination source and the

quality of the masks are the main issues to overcome. NIL uses template to contact print on wafers. Cross contamination problems still will be a fatal issue. ML2 uses electron beam system to direct write on wafers.

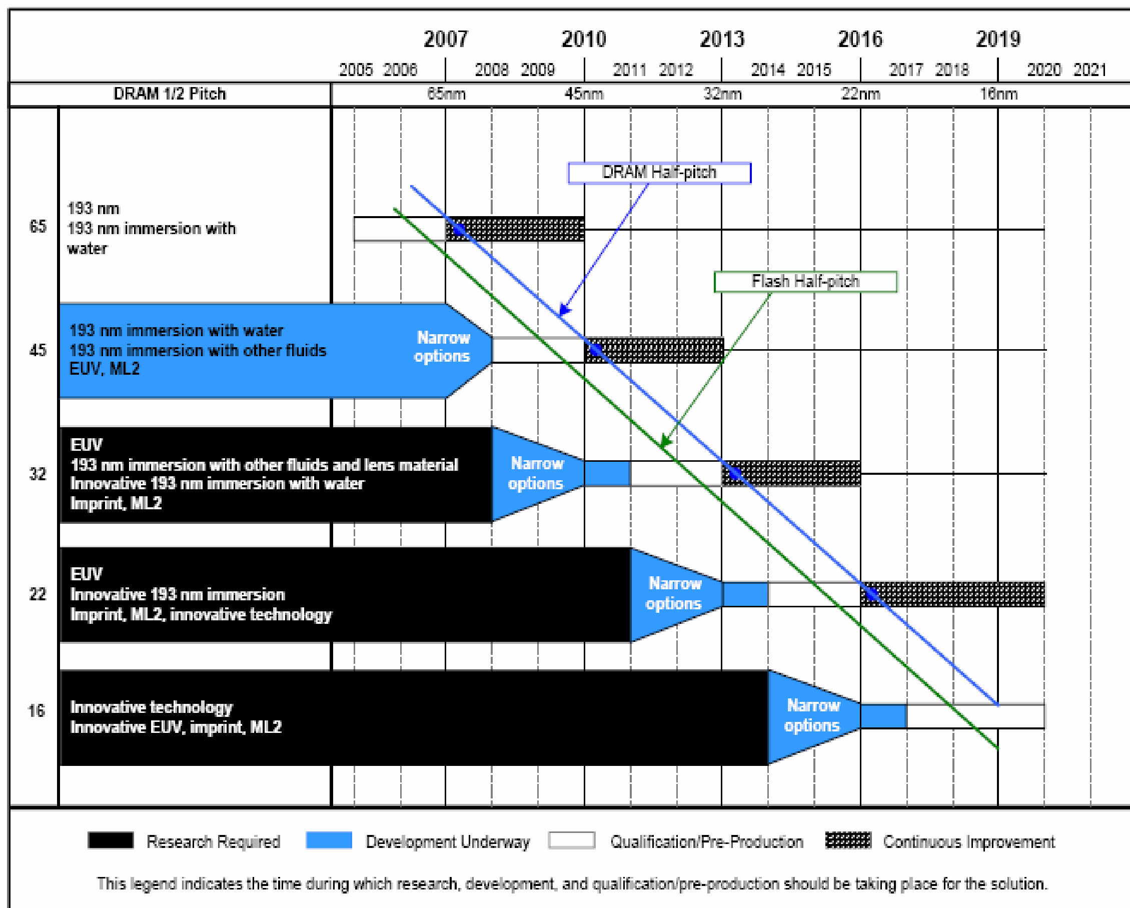

Fig 1-1 Potential lithography solution for next generation lithography from ITRS, Y2005 version [2].

Electron beam lithography system is a mature technology and has been used for about 50 years. E-beam system was evolved from SEM (Scanning electron microscope) and SEM was developed in 1955 [3]. E-Beam Lithography followed soon after the development of SEM and was one of the earliest processes used for IC fabrication dating back to 1957 [4]. Currently, E-beam lithography has two kinds of application. The first and the most frequently being used one is mask-making. The most advanced masks are all produced by E-beam exposure systems. The other application of E-beam exposure system is used to direct-write patterns on wafers. It can save cycle time and cost of mask-making, and provide quick delivery of chip making.

However, low throughput limits wide application of E-beam exposure systems. In 1976, Webber and Moore et al. used variable spot shaping to improve throughput of the system [5]. Many E-beam exposure systems vendors had proposed many methods to improve the throughput for this forty years. But the throughput still failed to compare to optical lens projection system. Most efforts of E-beam exposure system vendors still focus on the

throughput improvement. To further improve the throughput of the systems, many new techniques are under being developed. The new techniques include multi electron-guns system [6], multi lens system [7] and projection mask-less lithography (PML2) [8] et al. The evolution of E-beam system is shown at Fig 1-2 [9].

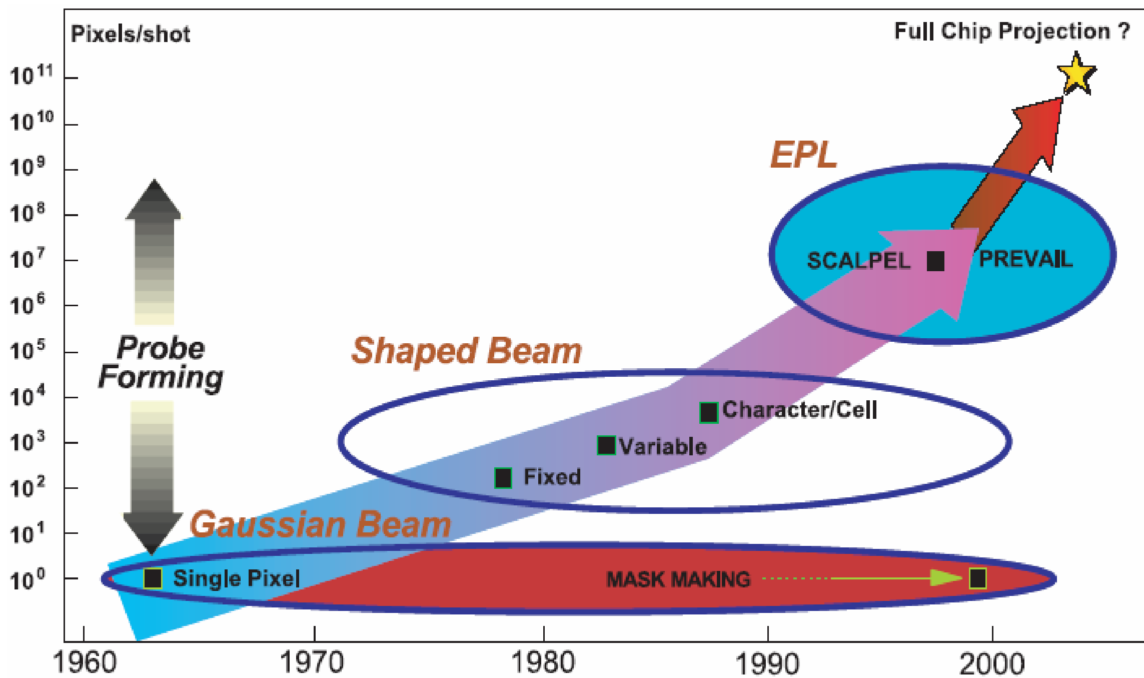

Fig 1-2 E-beam lithography evolution [9].

Besides, there are some annoying effects, including charging effect, heating effect and proximity effect. The proximity effect is the most serious impact for E-beam exposure lithography. It makes pattern's CD (critical dimension) difficult to control and often makes exposed patterns lose fidelity. When performing e-beam exposure, electrons make interactions with the atoms of bombardment target and are scattered away by the atoms randomly. The scattering interactions are characterized as forward and backward scatterings. To quantify the scattering effects and to make adequate correction are important and necessary to improve performance of E-beam lithography, especially for nanotechnology. The proximity effect correction parameters for each structure will be obtained before making corrections.

In chapter 2, electron-slid interaction will be introduced. It will include proximity effect issues and the correction methods. In chapter 3, our developed Monte Carlo simulation program will be described. The verification procedure and result will also be provided. And simulation of different structures will also be included. In chapter 4, proximity effect parameters extracted from experiment data will be mentioned. The exposure results with proximity effect correction and discussion will also be provided. We will make our conclusion in chapter 5. The future work for this study will also be included there.

Chapter 2. Electron interaction of E-beam lithography

Electrons interact with the bombarded films or under layer substrate during an E-beam exposure process. During the process, the photoresist film will be deposited energy from the dissipation energy of incident electron and form an exposure image. For example, when exposing a negative resist film, the exposed area of the photoresist film will form an energized image and will not be developed away and form a photoresist patterns for further process. But there are some electrons scattered back from the intermedium films or the substrate. The deposited energy of the backscattered electrons depends on the types of under layer films and substrate. Besides, it is very strongly depends on the pattern density of nearby exposed area and it is the so called proximity effect. To know the proximity effect clearly and to correct the proximity effect adequately are necessary to get good control of E-beam lithography. Some of the famous proximity effect parameters extraction methods and proximity effect correction methods will be reviewed in this chapter.

2.1. Electron scattering processes

The scattering processes can be classified as elastic interactions and inelastic interactions. When the incoming electron interacts with a nucleus, it will be scattered away with significant change of direction and negligible energy loss because of the large mass difference between electron and nucleus. As the incoming electron interacts with the surrounding electrons of atom, it will cause inelastic interaction. The interaction will cause significant energy loss with negligible direction change.

In case of E-beam lithography exposure process, the top film will be the photoresist film. There is always an intermedium film between the top film and the bottom bulk. And silicon crystal substrates are the most often used substrates for semiconductor manufacturing. As the energized electron impinges on the photoresist film, it will penetrate the photoresist film and be scattered by the atoms of the film and undergoes a complicated scattering process. The electron trajectories can be approximated by a classical zigzag path. Most electrons will penetrate to the

bulk and stop there like path 1 in Fig 2-1.Some of the penetrated electrons will be scattered backward to the photoresist film like path 2 in Fig 2-1. The electron will lose energy during the traveling path and finally stopped when it lose all of its kinetic energy.

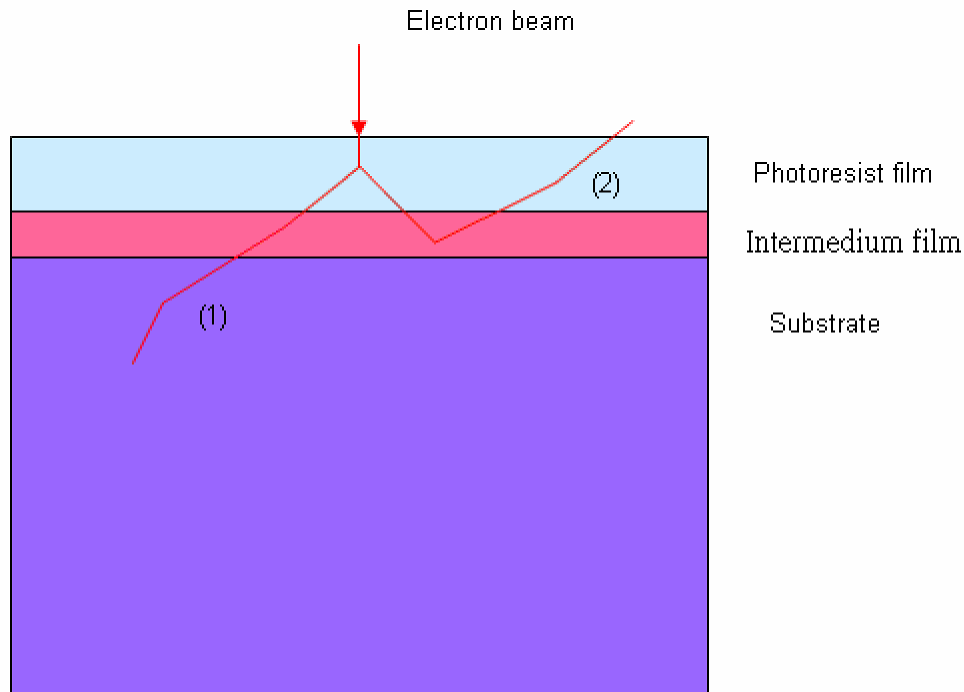

Fig 2-1 Electrons trajectories schema to show electron scattering path of E-beam lithography.

2.2. Proximity effect

As electrons bombarded photo-resist film, there will be many scattering events before the electrons enter the substrate. This type of scattering is characterized as forward scattering. And the deposited energy in photoresist is known as forward scattered energy. We can model this deposited energy by a normal distribution function. Most of the electrons will penetrate the photo-resist film and enter the substrate. The incident electron will lose most energy during the path of the substrate. Some of the penetrating electrons will scattered backward to the photoresist film. The backscattered electron also gives energy to the photoresist film. And the energy was called backward scattering energy. The exposure intensity distribution of point exposure is often expressed as the double Gaussian functions:

$$f(r) = \frac{1}{\pi(1+\eta_E)}\left[\frac{1}{\alpha^2} e^{-(\frac{r}{\alpha})^2} + \frac{\eta_E}{\beta^2} e^{-(\frac{r}{\beta})^2}\right] \tag{2.1}$$

where r is the distance to the E-beam exposure point. η_E is the ratio of backscattered energy to forward scattering and α is the distribution range of forward scattering range and β is the distribution range of backward scattering. The double Gaussian functions were first proposed by T.H.P Chang to describe the distribution of deposited energy of E-beam exposure in 1975 [10].

In 1987, S.J. Wind et al. introduced triple Gaussian functions to describe the distribution for sub-100 nm features [11]. It can better fit the deposited energy distribution. Some other kinds of triple functions were also proposed [12, 13]. But currently commercial proximity effect correction software packages, for example PROXECCO and CAPROX, mostly use double Gaussian functions parameters to correct the proximity effect. So we chose to use double Gaussian proximity effect functions through the thesis.

As two E-beam exposed patterns are too close to each other, the backscattered energy will be added to each other respectively. This unwanted and annoying effect is so called proximity effect and it always makes the E-beam exposure difficult to control. The backscattered range depends on the structure of the bombarded target and it is about 1 to 10 μm. For sub μm patterns, the proximity effect is one of the most serious problems for E-beam lithography. From Fig 2-2 (b), we can clearly see the troublesome proximity effect. Originally, there are 2 sets of two coarse and nearby lines and three fine and sparse lines of designed patterns as shown in Fig 2-2 (a). The simulated exposed result without proximity effect correction at Fig 2-2 (b) shows that there are unwanted bridges between the coarse lines due to the proximity effect. And the sparse lines were wrongly opened at the center of the lines for not enough deposited energy. This explains the basic phenomenon of proximity effect.

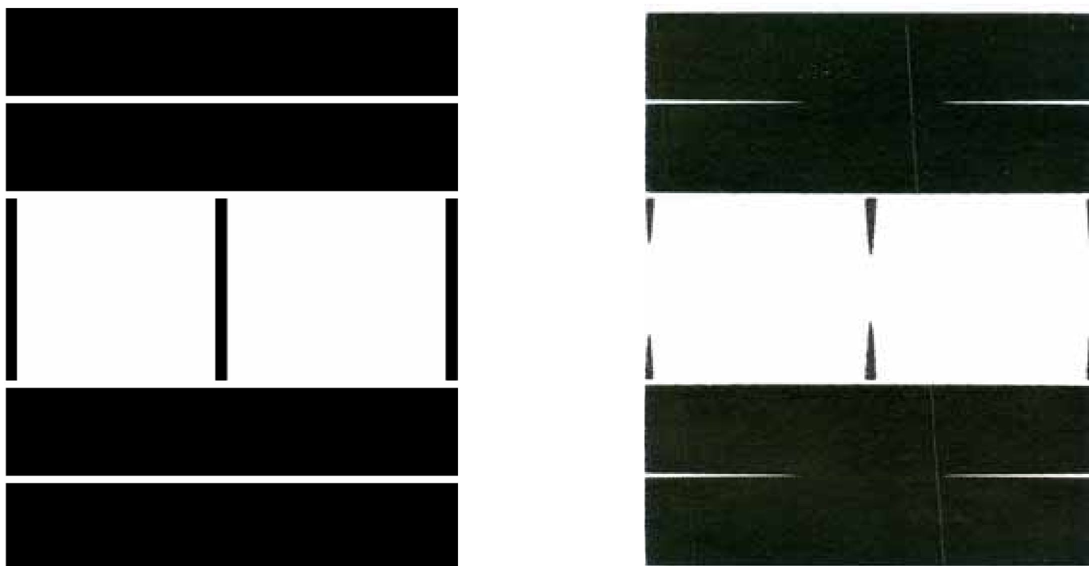

Fig 2-2 Test patterns for proximity effect and simulation result (a)Designed test patterns for checking proximity effect (b) Simulated result of uncorrected proximity effect exposure [14].

2.3. Proximity effect correction

In most cases, proximity effect is corrected by dosage correction of the exposed patterns. Proximity effect parameters and patterns' file are inputted into proximity correction software and a corrected exposure file was generated. The corrected exposure file will be read by the E-beam exposure tool to expose the wafers. To prepare adequate proximity effect parameters for every exposed structure in advanced is necessary to correct the proximity effect for dosage correction method.

2.3.1. Proximity effect parameters

There are various methods to obtain the proximity effect parameters including empirical methods and PC simulation methods. Famous empirical methods are doughnut type and point type etc. After measurement of the developed wafers, proximity effect parameters could be extracted or fitted from the experiment data. They also could be obtained from PC simulation. Monte Carlo simulation method is the most often used one. Besides, N. Glezos and I. Raptis et al, developed a simulator based on the Boltzmann transport equation to obtain the proximity effect parameters [17, 18].

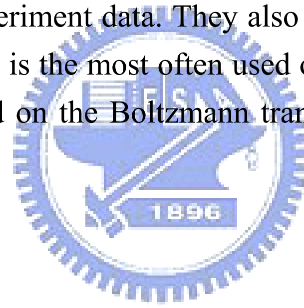

2.3.1.1. Doughnut Type

This method uses a test pattern consisting of a set of rings (doughnuts) with variable inner radius and large but constant outer radius. The evaluation of the exposure after development can easily be done by optical microscope [15]. A test cell of the exposure pattern is shown at Fig 2-3. R1 is the radius of inner circle and is variable. R2 is the radius of outer circle and is kept constant and much larger than the backscattered range. At the center of the inner circle, point P, the effective dose is

$$\begin{aligned} Q_p &= Q\int_{R_1}^{R_2} 2\pi r f(r)dr = D_0 \\ &= \frac{2\pi Q}{1+\eta}[\exp(-(\frac{R_1}{\alpha})^2) + \exp(-(\frac{R_1}{\beta})^2)] \end{aligned} \tag{2.2}$$

where f(r) is the proximity effect function. D_0 is the threshold energy, Q is the exposed dosage,

α, β and η are proximity effect parameters of the proximity effect function. After E-beam exposure and development of this matrix, the evaluation procedure consists of the identification for each dose which inner circle was just cleared out (in case of a positive resist). The proximity effect parameters can be extracted hereafter. The advantage of this method is that no SEM measurement was needed. The main disadvantage of the method is that exposed patterns are seldom designed like a plate or ring in IC layout. It can't adequately reflect the true phenomenon of E-beam exposure.

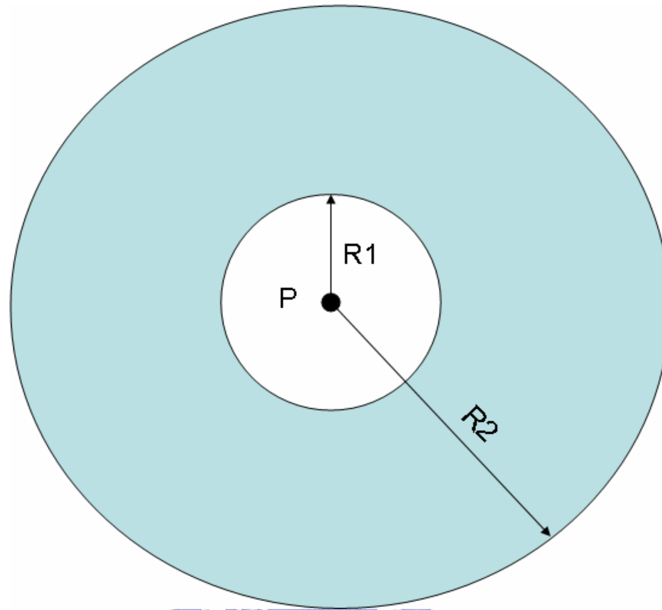

Fig 2-3 Test cell of the Doughnut-method [15]. R1 is variable while R2 is fixed and much larger than backward scattering range.

2.3.1.2. Point Type

Sequences of single point exposure are made for pint type method to extract proximity effect parameters [12]. Each point receives about 20% more exposure dosage than the preceding one. The sharply defined clearing threshold is obtained at a different radius in each of the point exposure. The radii are easily measured by scanning electron microscope. The normalized distribution is thus obtained and shown at Fig 2-4. The proximity effect parameters could be fitted from the normalized distribution. The main advantage of the method is that it can reflect the deposited energy on photoresist film after E-beam exposure of point pattern. The main disadvantage of the method is that exposed patterns are seldom designed this type, too. The fitted proximity effect parameters of double Gaussian functions can not exactly correct the proximity effect error.

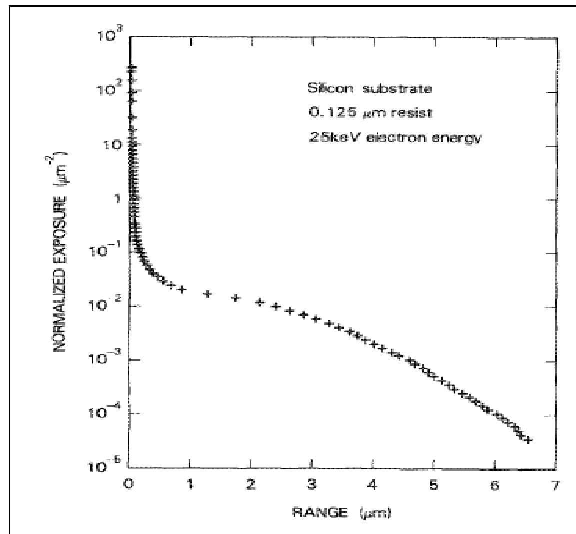

Fig 2-4 Normalized exposure on silicon at 25 KeV by point exposure method [12].

2.3.1.3. SCELETON

Sceleton is a commercial Monte Carlo simulator. It performs a Monte Carlo simulation of electron trajectories in arbitrarily complex material stacks. The calculated radial energy density distribution (point spread) can be used directly as input for the proximity correction program PROXECCO, resist profile simulation tools. Monte Carlo simulation is carried out using a single scattering model, where the electron trajectory is followed through a series of scattering events in the resist/substrate stack. Elastic scattering events are described using the screened Rutherford formula. Energy dissipation due to inelastic scattering is modeled by Bethe's energy loss formula in the continuously slowing down approximation (CSDA). Currently, Sceleton needs to perform at work station platform and it does not provide PC version yet [16].

2.4. Proximity effect correction methods

2.4.1. Dose correction

CAPROX (computer aided proximity correction) makes local corrections to structure or variants of structures [19]. The locality to which the correction is applied may be any structure. Parikh’s self consistent solution [20] was adopted. A fracturing is performed prior to solving

the set of integral equations.

PROXECCO (Proximity effect correction by convolution) is used to correct proximity effect. It separates the calculation into correction-related and pattern-related steps [14]. The resolution of the correction does not depend on pattern dimension. Coarse grids are sufficient. The time needed for transformation turns out to be comparable to the time needed for data treatment [14]. PROXECCO were used for the proximity effect correction for our study. The following figures show the corrected patterns and simulation result with this correction method. At Fig 2-5 (a), the different gray levels indicate different dosage needed for E-beam exposure. At Fig 2-5 (b) shows the simulation deposited energy of the corrected exposure.

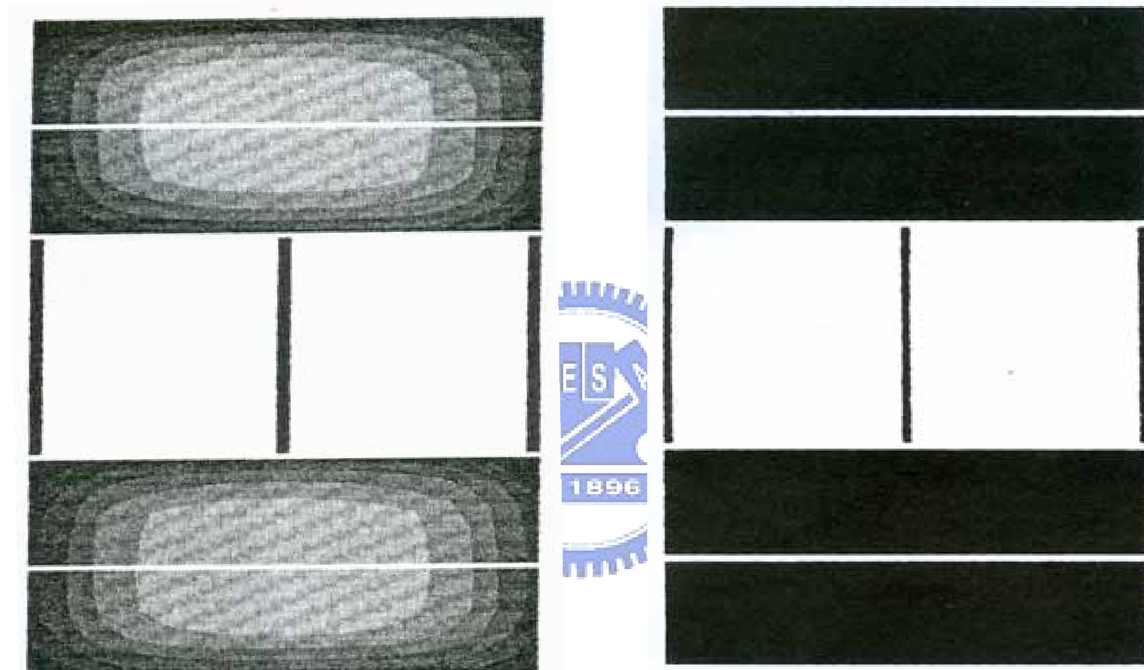

Fig 2-5 (a) Pattern corrected by PROXECCO with coarse resolution. (b)Simulation exposed result of PROXECCO with coarse resolution correction [14].

2.4.2. Shape compensation

Shapes of the intended exposed patterns are modified in this method and the dosage for each exposed point is kept constant. An example of a shape modification method is shown at Fig 2-6 and it is a correction scheme in PYRAMID [22]. The pattern is adjusted via pre-calculated rule tables. The major disadvantage is that experiment data is needed to obtain the necessary rule tables. And the throughput will be impacted due to more fractures or small pixel of E-beam.

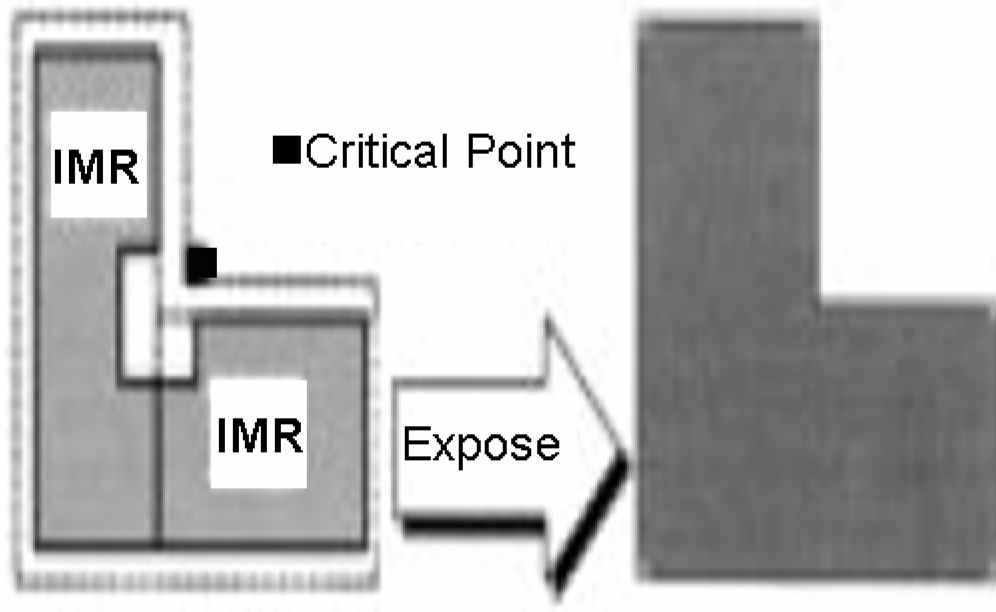

Fig 2-6 Graphical illustration of IMR (inner maximum rectangular) adjustment and shape correction at corner and its simulated correction effect [22]. The left part is the modified exposure pattern, the right part is the simulation result of deposited energy .

1896

2.4.3. Background correction

Background exposure correction is often referred to as GHOST method. It works by writing a second exposure which is the inverse of the intended image and the electron beam is defocused. Fig 2-7 shows the working principle of this method. The scheme works by equaling the background electron energy dose received by all points within the pattern [21]. The major advantage is that this method works without proximity effect correction. The main problem is that the correction exposure can not exactly mimic the inverse of the intended image. And the loss of throughput due to double exposure is another drawback.

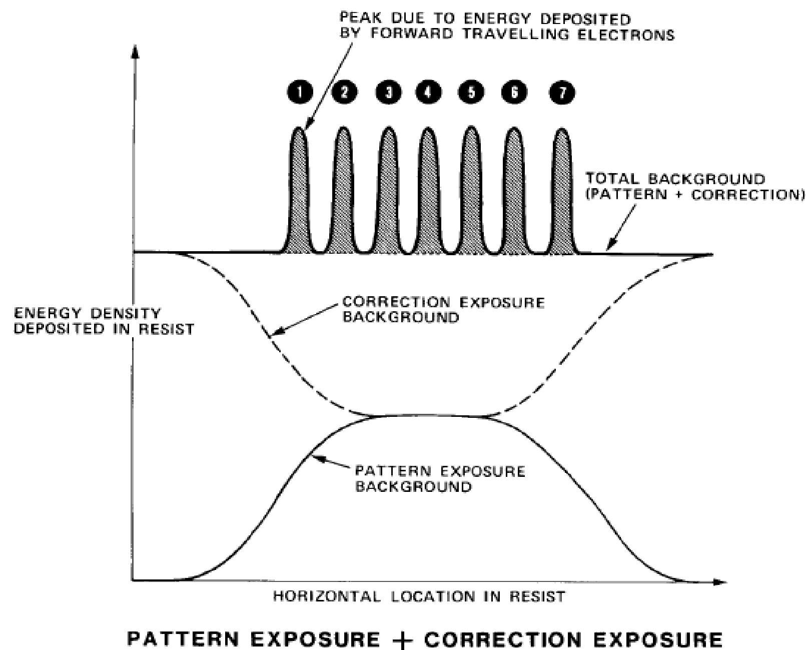

Fig 2-7 Energy distribution of combination of pattern exposure and correction exposure [21].

2.4.4. Top surface image method

The Bethe range of an electron is the total length of path one energized electron can travel before it stopped or reach cut off energy. The Bethe range of polymer material is short for low accelerated voltage electron. For example, the range for PMMA of 5KeV electron is only 0.64 μm [23]. If the thickness of photoresist is larger than half of the electron range, the backscattered electron from substrate will not reach top surface of the photoresist film. The similar phenomena will happen for multi-layer resist structure. For this reason, top surface image technique of high thickness resist or multi-layers resist will be a good solution for low energy E-beam exposure lithography [24, 33]. The major advantage is that no proximity effect correction is necessary. The disadvantage is the increased process complexity. Fig 2-8 shows a typical patterning process of the top surface image technique.

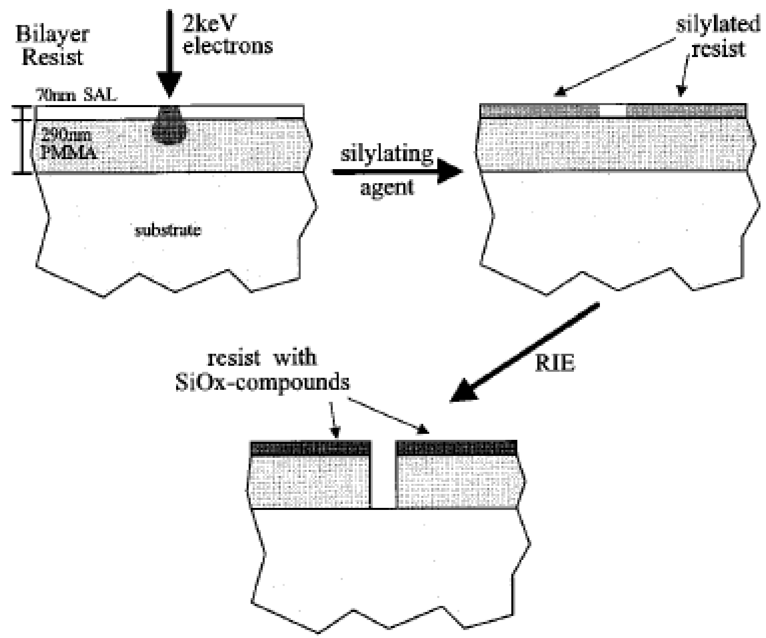

Fig 2-8 A bi-layer process using top surface image of low energy E-beam lithography to alleviate proximity effect [33].

Chapter 3.

Monte Carlo simulation for E-beam lithography

In this chapter, Monte Carlo method will be mentioned. It includes various Monte Carlo models and a simulation program which was developed based on the single scattering model. The verification of the simulation program was also included. And the proximity effect parameters for the test structures were also obtained by the developed simulation program.

3.1. Monte Carlo Models

There are various models of Monte Carlo simulation for electron interactions, including multiple scattering model, single scattering model, hybrid model, direct simulation model and dielectric function model [25].

3.1.1. Multiple scattering model

Multiple scattering model was initiated by Berger (1963) for practical Monte Carlo calculations of penetrated of charged particles in matter [25]. It was based on the use of Bethe's stopping power equation describing energy loss and angular distribution for electron scattering from transport equation.

3.1.2. Single scattering model

Single scattering model adopts the screened Rutherford scattering cross section in place of the angular distribution [25]. The energy loss is given by Bethe's stopping power equation as in the multiple scattering model. It is widely used and suitable for energy dissipation of E-beam lithography.

3.1.3. Hybrid model

Hybrid model initially was proposed by Schneider and Cormack (1959) for the discrete and continuous energy loss processes [25]. It has done much to extend Monte Carlo calculations to alloys and compound materials including secondary electron generation.

3.1.4. Direct simulation model

Direct simulation model is probably the most basic approach leading to a more comprehensive understanding of the various excitations associated with electron penetration [25]. However, it requires exact knowledge of individual inelastic scattering, and this is available for only a few materials.

3.1.5. Dielectric function model

Dielectric function model is based on use of the Mott scattering cross-section and the dielectric function describing elastic and inelastic process, respectively [25]. It is applicable to low energy electron as to high-energy electrons. The disadvantage is that the multiple-variable excitation function requires a large amount of memory for a practical computer simulation.

3.2. Electron interaction with atom

The accelerated electrons impacting on the target surface suffer elastic and inelastic collisions with the atoms of the impacted film via Coulomb forces. Elastic collision deflects the direction of the incident electron and happens when the electron collides with the nuclei of the atoms. On the other way, inelastic collision mainly causes loss of the kinetic energy of the incident electron when the incident electron interacts with the surrounding electrons of the atoms.

3.2.1. Elastic collision

As one electron interacting with the nucleus of an atom, the incident electron will be scattered with direction change and negligible energy loss. The angle of scattering can be calculated by

differential scattering cross section and Monte Carlo simulation. First, the differential scattering cross section should be analyzed. The calculation of differential scattering cross section was based on Born approximation and shielded Coulomb potential method. The shielded Coulomb potential and corrected screened length are given as

$$V(r) = \frac{Ze^2}{4\pi\varepsilon_0 r}\exp(-\frac{r}{d}) \tag{3.1}$$

where

$$d = \frac{0.885a_0}{1.12Z^{1/3}} \tag{3.2}$$

and Z is the atomic number of the target atom., e is the electric charge of an electron, a_0 is the Bohr radius, and d is the corrected length [26]. And the standard form of Born approximation is

$$f(\theta) = -\frac{2m}{\hbar^2 K}\int_0^\infty drrV(r)\sin Kr \tag{3.3}$$

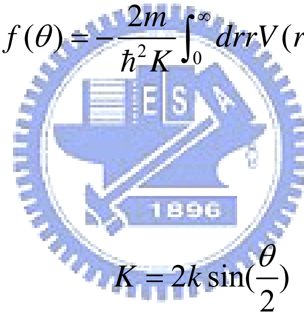

where

$$K = 2k\sin(\frac{\theta}{2}) \tag{3.4}$$

and k is the wave factor of the incident electron, θ is the angle change of the electron after scattering. Substituting the shielded Coulomb potential into the standard Born potential gives

$$\begin{aligned} f(\theta) &= \frac{2mZe^2}{4\pi\varepsilon_0\hbar^2 K}\int_0^\infty \exp(-r/d)\sin Krdr \\ &= \frac{2mZe^2}{4\pi\varepsilon_0\hbar^2}\frac{1}{K^2+(1/d)^2}, \end{aligned} \tag{3.5}$$

The corresponding differential scattering cross section is

$$\begin{aligned} \frac{d\sigma}{d\Omega} &= |f(\theta)|^2 \\ &= \frac{(mZe^2)^2}{(2\pi\varepsilon_0\hbar^2)^2}\frac{1}{[K^2+(1/d)^2]^2} \end{aligned} \tag{3.6}$$

where σ is the scattering cross section and Ω is the solid angle of the scattering. Substitution of equation (3.4) into (3.6) ,we get

$$\begin{aligned}
\frac{d\sigma}{d\Omega} &= \frac{(mZe^2)^2}{(2\pi\varepsilon_0\hbar^2)^2}\frac{1}{\left[(2k\sin\frac{\theta}{2})^2+\frac{1}{d^2}\right]^2} \\
&= \frac{(mZe^2)^2}{(4\pi\varepsilon_0\hbar^2k^2)^2}\frac{1}{\left[1-\cos\theta+\frac{1}{2d^2k^2}\right]^2} \qquad (3.7) \\
&= \frac{Z^2}{2^2\cdot(\frac{\hbar^2k^2}{2m})^2}(\frac{e^2}{4\pi\varepsilon_0})^2\frac{1}{\left[1-\cos\theta+\frac{1}{2d^2k^2}\right]^2}
\end{aligned}$$

The kinetic energy of electron is

$$E = \frac{\hbar^2k^2}{2m} \qquad (3.8)$$

Using equation (3.8) in (3.7), we get

$$\frac{d\sigma}{d\Omega} = (\frac{Z}{2E})^2(\frac{e^2}{4\pi\varepsilon_0})^2\frac{1}{\left[1-\cos\theta+\frac{1}{2d^2k^2}\right]^2} \qquad (3.9)$$

The total elastic cross section can be obtained by integration as

$$\sigma = \int_0^{2\pi}\int_0^{\pi}(\frac{Z}{2E})^2(\frac{e^2}{4\pi\varepsilon_0})^2(\frac{1}{1-\cos\theta+2\mu})^2\sin\theta d\theta d\phi \qquad (3.10)$$

where

$$\mu = \frac{1}{4d^2k^2} \qquad (3.11)$$

and μ represents the effective screening parameter of the electron cloud. The equation becomes

$$\sigma = 2\pi\int_0^{\pi}(\frac{Z}{2E})^2(\frac{e^2}{4\pi\varepsilon_0})^2(\frac{1}{1-\cos\theta+2\mu})^2\sin\theta d\theta$$
$$= (\frac{Ze^2}{8\pi\varepsilon_0 E})^2(\frac{\pi}{\mu(\mu+1)}) \quad (3.12)$$

To take into account of inelastic scattering, Z^2 is replaced by Z(Z+1) [27]. The total scattering cross section becomes

$$\sigma = (\frac{e^2}{8\pi\varepsilon_0 E})^2(\frac{Z(Z+1)\pi}{\mu(\mu+1)}) \quad (3.13)$$

3.2.2. Inelastic collision

Between elastic scattering events with nuclei, the incident electron is assumed to interact with the surrounding electrons of the nearby atoms. And it will lose kinetic energy during the traveling path. This energy loss is usually modeled by the Bethe continuous slowing down approximation [23] as

$$\frac{dE}{ds} = -2\pi(\frac{e^2}{4\pi\varepsilon_0})^2\frac{NZ}{E}\ln(\frac{\gamma E}{J}) \quad (3.14)$$

where N is the atoms number density of the target, γ=1.1658 is a constant, and J represents the mean excitation energy in the solid.

3.3. PC simulation

The simulation program was implemented with VC++ and run in Pentium-4 personal computer. The random numbers files were downloaded from random organization [28] instead of pseudo random numbers to get adequate randomness. Several thousands random numbers were served for one incident electron of 40 KeV.

3.3.1. Density calculation

The density of the photoresist is necessary for the simulation of electron bombardment. We used electronic balance, AG285, to measure masses of 3 pieces of 6 inches wafers before coating. Then measure the same 3 wafers after spin coating with NEB-A4 photoresist.

The photoresist thickness was measured at n&k tool, NKT-1500. The edge bead removal width of spin coating is 2 mm. The cover area per wafer can be calculated. The density of the coated photoresist can be obtained by following equation as

$$d = \frac{M_{after} - M_{before}}{3 \times A \times t} \tag{3.15}$$

where d is the density of the photoresist film to be calculated, A is the calculated photoresist covered area of one coated wafer, t is the averaged measured thickness of the photoresist film, M_{after} and M_{before} are the measured masses of the wafers after and before spin-coating respectively.

3.3.2. Components analysis

It is important to know the composition of the photoresist film before simulation. ESCA (electron spectroscopy for chemical analysis) was used to analyze the photoresist film components. ESCA can't analyze hydrogen. So we used EA (Elemental Analyzer) for hydrogen ratio analysis. The ESCA result is shown at Fig 3-1 and Table 3-1. The EA result is shown at Table 3-2.

1896

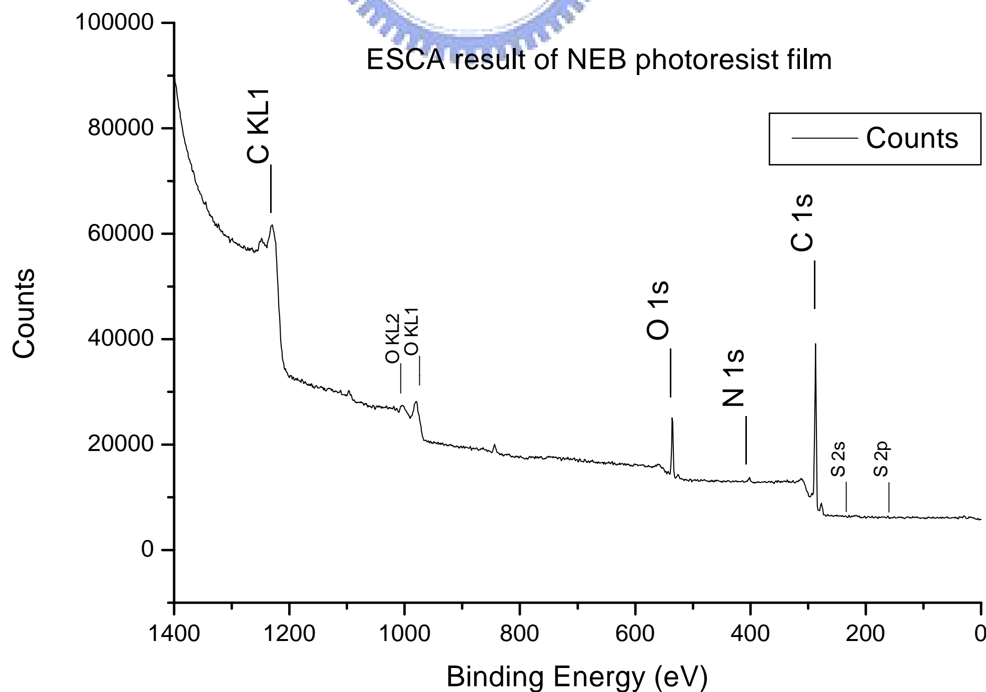

Fig 3-1 ESCA spectrum for NEB-A4 photo-resist film. The elements for the analysis are C,O,N and S.

Table 3-1 atomic percentage of NEB-A4 photo-resist film derived from ESCA.

Element	AT%
O	11.886
C	1.862
N	85.903
S	0.349

Table 3-2 Atomic weight percentage of elements in photoresist NEB-A4 obtained from EA.

	N %	C %	H %
Exp-1	2.55	71.66	7.03
Exp-2	2.50	71.50	7.22
Average	2.52	71.58	7.17

3.3.3. Mean free path random number R1

The mean free path between collisions could be obtained as [23]

$$\lambda = (\sum_i n_i \sigma_i)^{-1} \tag{3.16}$$

where σ_i is the total scattering cross section of ith species and is given at equation (3.17). Using a random number, the distance s an electron travels between the collisions is

$$s = -\lambda \ln R_1, \tag{3.18}$$

where R_1 is a random number read from random number file.

3.3.4. Scattering center atom random number R2

The probability of scattering of an atom of the ith species is [23]

$$P_i = \frac{(n_i \sigma_i)}{\sum_i n_i \sigma_i} \tag{3.19}$$

where n_i is the atom number density of ith species and σ_i is the total scattering cross section of ith species. The scattering center is chosen to be n^{th} species when the following equation is met.

$$\sum_{n=i} P_n < R_2 \le \sum_{n=i+1} P_n \tag{3.20}$$

3.3.5. Angle of scattering random number R3

The probability of scattering angle is lied between 0 and π. And it can be obtained from

$$\begin{aligned} R_3 &= \frac{\int_0^\theta \frac{d\sigma}{d\Omega} \sin\theta d\theta}{\int_0^\pi \frac{d\sigma}{d\Omega} \sin\theta d\theta} \\ &= (\mu+1)(\frac{1-\cos\theta}{1-\cos\theta+2\mu}) \end{aligned} \tag{3.21}$$

where θ is the calculated change of angle of the scattered electron. From (3.22), we can get

$$\cos\theta = 1 - \frac{2\mu R_3}{1+\mu-R_3} \tag{3.23}$$

, and the scattering angle could be obtained from this equation.

3.3.6. Azimuthal angle random number R4

The azimuthal angle Φ is equally spanned between 0 and 2π. It can be easily obtained from

random number as [23]

$$\Phi = 2\pi R_4 \tag{3.24}$$

3.3.7. Trajectory of scattering

As mean free path, *i*th species scattering center, θ and Φ are decided, one can calculate the next position and direction of the impinged electron. And the electron will lose kinetic energy during the path. It will repeat and repeat until the electron lost enough energy to reach cut off energy [23]. One step of the electron trajectory is shown at Fig 3-2.

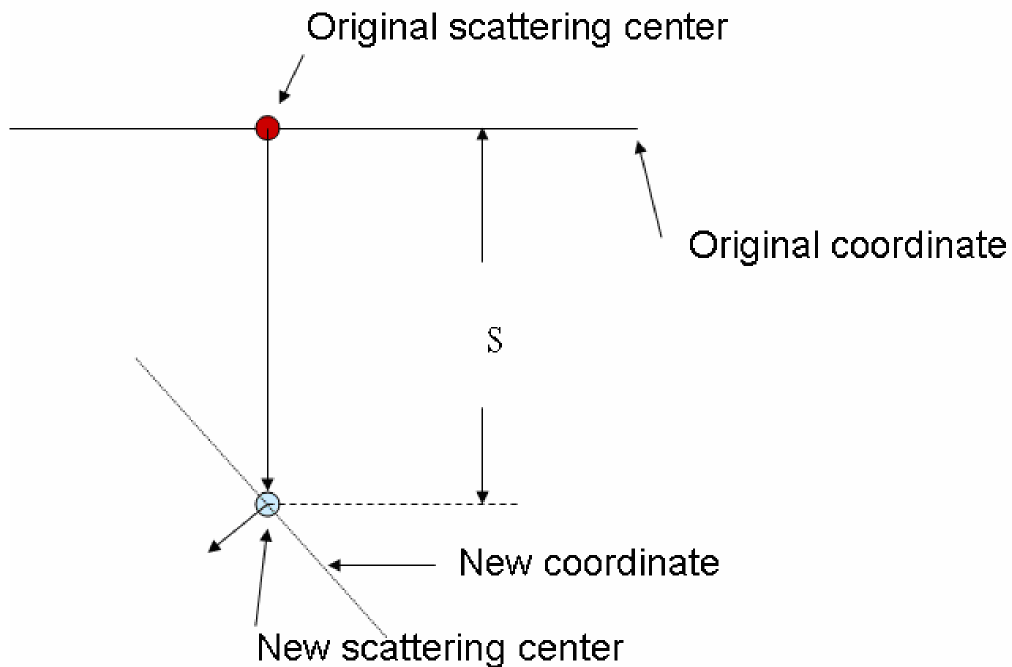

Fig 3-2 One step of electron movement in 2D schematic drawing.

3.4. Verification

To verify correctness of the simulation program, comparison of stopping power, penetration ratio, reflection ratio and energy profile will be done. PMMA (polymethyl methacrylate, $C_5H_8O_2$) film on silicon substrate was mostly frequently used for simulation, test, and comparison. For energy profile, PMMA film on blank mask plate was used for simulation and comparison.

3.4.1. Stopping power

The incident energized electron will lose power when inelastic interaction occurs during the bombardment process. Continuous slowing down approximation formula is used to calculate the lost power. Stopping power is the lost power per unit length of the incident electron. It depends on the electron energy and the film that the electron traveling.

Stopping power of the films could be verified by the stopping range, Bethe electron range, of the energized electron. Stopping range is the length of path one energized electron could travel before it reached cut off energy. The cut off energy was assumed 500 V during the test [23]. Stopping range depends on the material of the bombarded target and the energy of the incident electron. Higher energized electrons get longer stopping range. Film of low atomic number elements or lower density gets longer stopping range. The result was compared with the reference paper [23], and listed at Table 3-3.

Table 3-3 Verification of stopping range of different accelerated voltage of PMMA and silicon.

material	Accelerating Voltage	Bethe electron Range Calculated (μm)	Bethe electron Range Compared [24]	Deviation percentage (%)
PMMA	5KeV	0.64	0.65	1.5
PMMA	10KeV	2.18	2.18	0
PMMA	20KeV	7.58	7.55	1
Si	5KeV	0.48	0.48	0
Si	10KeV	1.52	1.52	0
Si	20KeV	5.07	5.08	0.2

From Table 3-3, the result shows good consistency with the result from the reference paper [23]. The stopping power formula of our program was checked and verified to be correct.

3.4.2. Penetration and reflection ratio

For E-beam lithography, the incident electrons will first traveling at the top resist film. Almost all of them will penetrate to the under layer film or substrate. Some of the penetrating electron will be scattered back to the resist film by elastic collisions with the atoms of the substrate or intermedium film.

400 nm thickness of PMMA film on silicon substrate was used for simulation. 10000 counts of electrons were used for bombardment in the simulation. The penetration ratio is defined as the ratio of the number of electrons, entering under layer film or substrate at least once, to the total number of the incident electrons [23]. And the reflection ratio is defined as the ratio of the number of back-scattered electrons, entering resist film again from under layer film or substrate at least once, to the total number of incident electrons [23]. And the results are listed at Table 3-4 and Table 3-5.

Table 3-4 Comparison of penetration ratio of 400 nm PMMA on silicon substrate of different acceleration voltage 20KV, 10KV, 5KV.

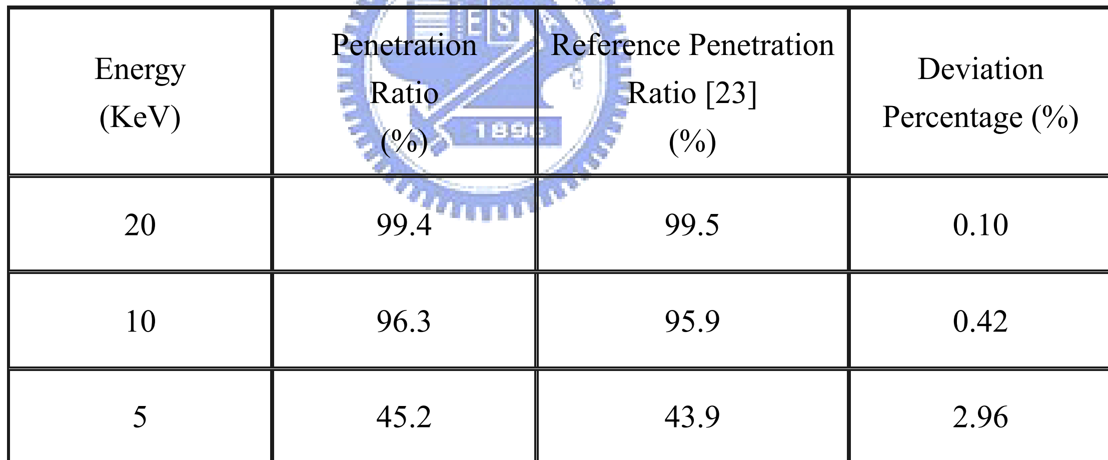

Energy (KeV)	Penetration Ratio (%)	Reference Penetration Ratio [23] (%)	Deviation Percentage (%)
20	99.4	99.5	0.10
10	96.3	95.9	0.42
5	45.2	43.9	2.96

From Table 3-4 and Table 3-5 , the penetration ratios and reflection ratios result shows consistent with the reference. The total elastic cross section formula and random variable of our simulation program are verified to be consistent with the reference.

Table 3-5 Comparison of reflection ratio of 400 nm PMMA on silicon substrate of different acceleration voltage 20KV, 10KV, 5KV.

Energy (KeV)	Reflection Ratio (%)	Reflection Ratio [23] (%)	Deviation Percentage (%)
20	18.3	18.2	0.5
10	23.2	24.2	4.1
5	29.1	30.1	3.3

3.4.3. Energy profile

Finally, constant energy contour was checked for the verification. In this test, 500 nm of PMMA resist film on 0.08 μm Cr film on a thick bulk SiO_2 substrate was used for simulation. 500 nm isolated line pattern were used. The incident electron energy for the test is 20 KeV and the dosage is 80 uc/cm^2. The patterns are simulated in terms of Gaussian sources at a density of 8 lines/μm (s=0.125 μm) and with a standard deviation σ=0.05 μm. This density was chosen that a 0.5 μm line would contain four beam positions. The constant energy contours of reference paper are dash lines shown at Fig 3-3. Due to symmetry to the line center, only the right half energy profile of the line is shown [30]. Constant energy contours of same energy of our developed program were shown at Fig 3-4.

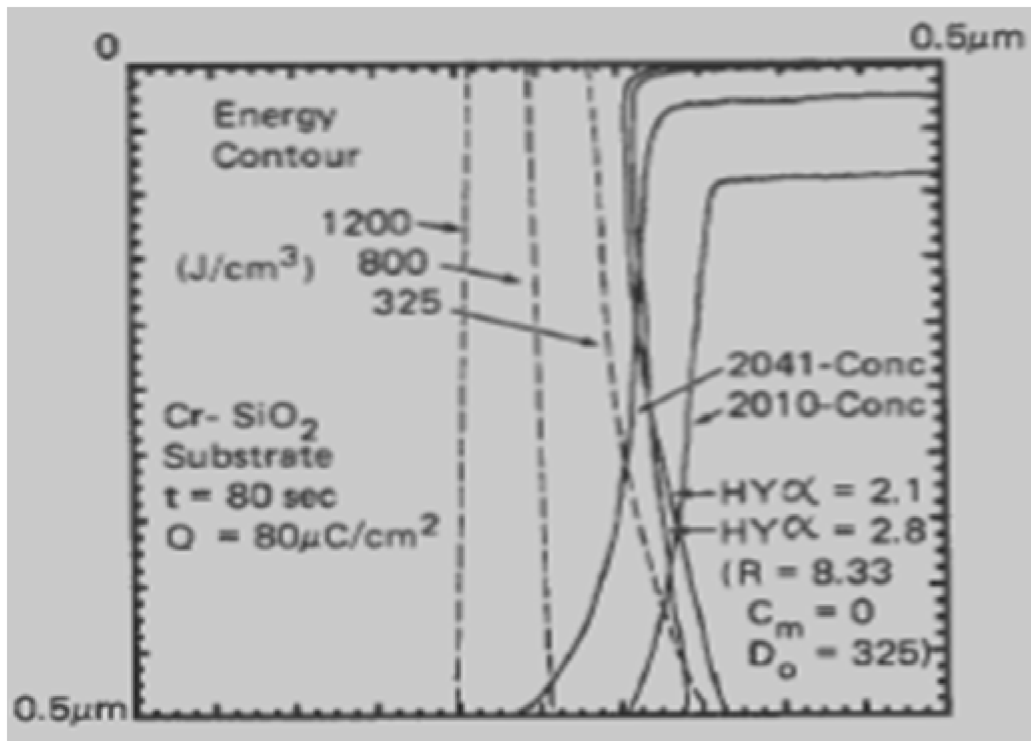

Fig 3-3 Constant energy density contour of 0.5 μm line for mask case. The source is Gaussian beam with 50nm range, at 20 KeV [30].

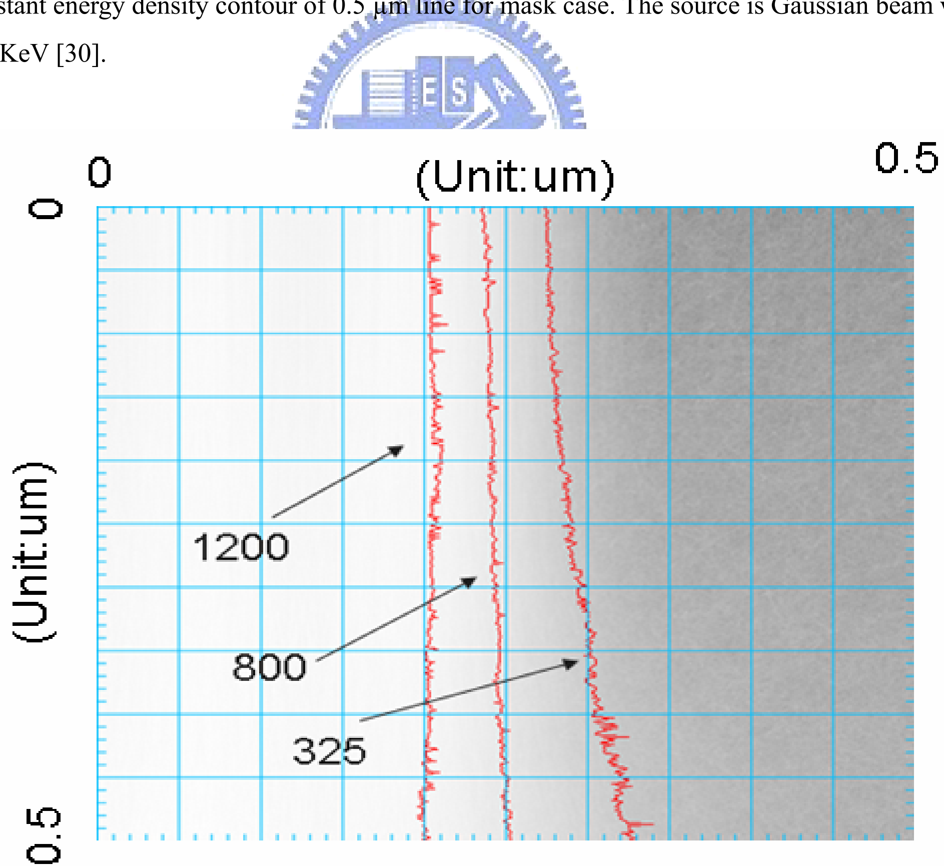

Fig 3-4 Simulation energy density contour of 0.5 μm line of our developed program. The source is Gaussian beam of range 50nm at 20KeV.

Three contours of constant energy, 1200, 800 and 325 J/cm^3, were compared between the reference paper and our simulation program. In Fig 3-4, the brighter region indicates higher energy density and vice versa. The test condition of the simulation follows the reference. Similar constant energy profiles were obtained as the reference. Thus we make sure that the deposition of energy of our simulation can successfully indicate the energy deposition for E-beam lithography.

3.5. Simulation result

3.5.1. Electron transverse path

The electron beam accelerating voltage of Leica WePrint-200 is 40KV. For example, when bombarding on a 400nm thickness of NEB photo-resist coating at silicon substrate, the electrons traverse path is simulated and shown as Fig 3-5.

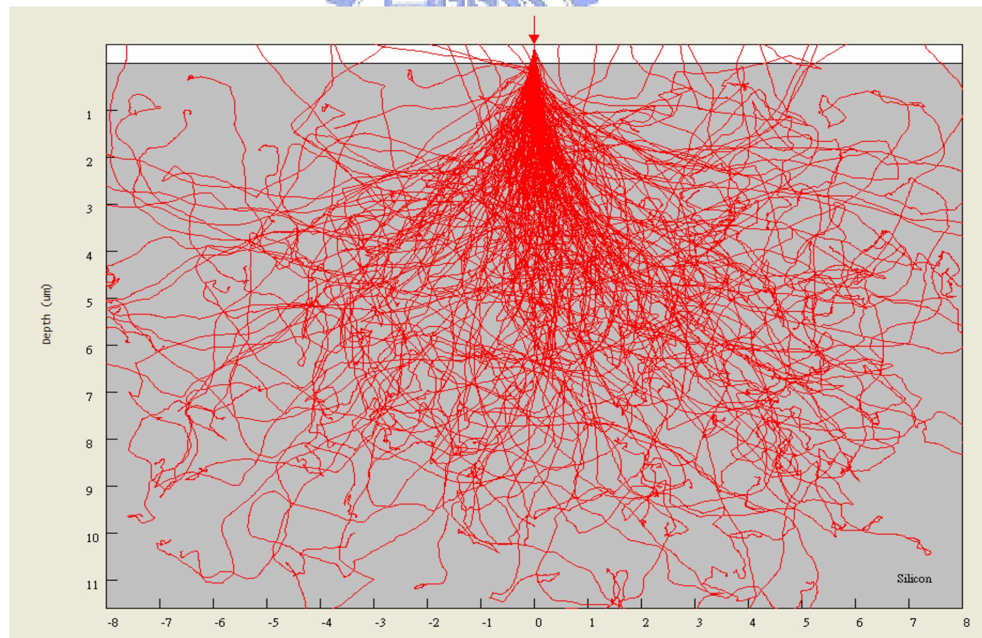

Fig 3-5 simulated electron path for 400 nm NEB film on Silicon substrate with 40KeV electron beam.

3.5.2. Energy parameter fitting

The forward and backward deposited energies were saved separately. The deposition energy of the bottom 50 nm region of photoresist film was used for further calculation [23]. The energy reflection ratio could be calculated as

$$\eta_E = \frac{\text{sum of backward energy of bottom 50 nm}}{\text{sum of forward energy of bottom 50 nm}} \tag{3.25}$$

The distribution range of forward energy and backward energy can be obtained using curve fitting tool of Matlab. For example, a backward energy fitting result of coating wafer on 1000nm copper with silicon substrate is shown at Fig 3-6.

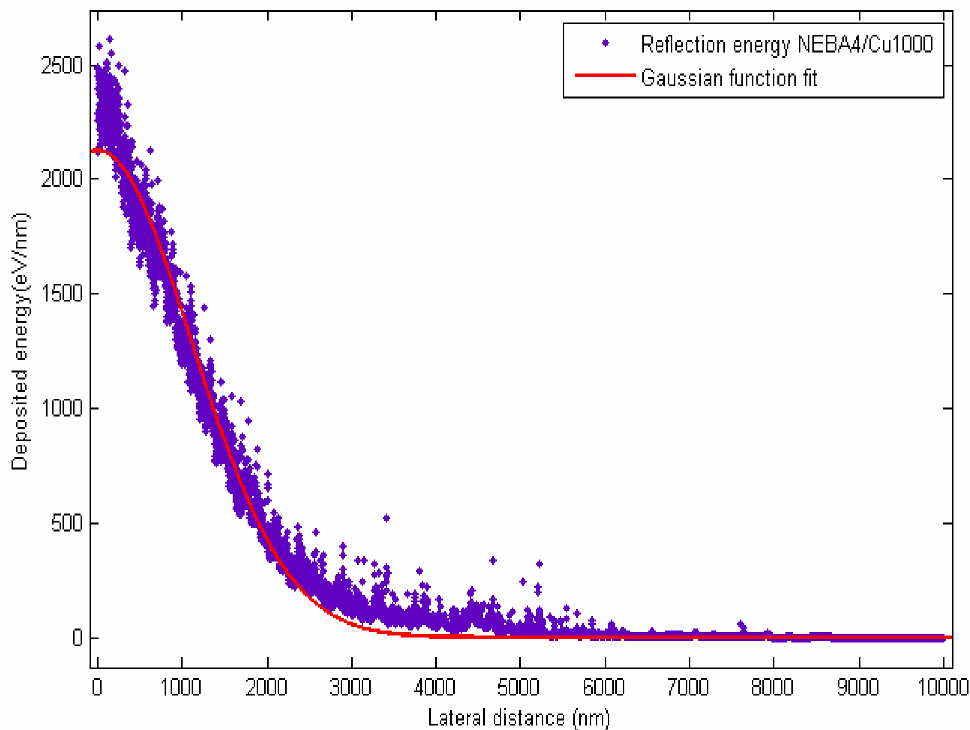

Fig 3-6 Gaussian fitting of backscattered energy of 40KV E-beam Exposure for 400nm NEB on 1000nm copper with silicon substrate.

3.6. Proximity effect parameters of Monte Carlo method

The proximity effect parameters, the reflection ratios and penetration ratios derived from the

Monte Carlo method are listed at Table 3-6. The forward scattering range is small compared to experiment fitting method. The backscattering ranges of the first 3 films are almost the same due to similar film averaged atoms mass and similar averaged atom number.

For same incident electron energy, from equation (3.13), the total cross section of an atom is nearly proportional to $Z^{4/3}$, where Z is the atomic number of scattering target. So the total cross section of Ta is the largest and the mean free path is the shortest. The backscattering range for Ta film is the smallest and the energy reflection ratio is the largest due to the largest atom number and the highest weight density.

Table 3-6 Test result of our developed Monte Carlo method for different film structures.

	Si-Substrate	SiO2_200nm	Si3N4_200nm	Ta300nm	Cu200nm
Average atomic number	14	10	10	73	29
Average atomic weight	28.09	20.03	20.04	180.9	63.55
Weight density (g/cm^3)	2.33	2.32	3.1	16.65	8.93
Atom density ($1/cm^3$)	4.98E22	6.95E22	9.28E22	5.52E22	8.43E22
Reflection Ratio	16168/ 100000	16279/ 10000	16250/ 100000	37056/ 100000	17924/ 100000
Penetration Ratio	99952/ 100000	99954/ 100000	99954/ 100000	99939/ 100000	99967/ 100000
Energy Reflection Ratio (150nm~ 199nm)	0.552	0.579	0.568	1.023	0.574
α (nm)	1.14	1.15	1.14	1.15	1.15
β (μm)	6.630	6.646	6.657	0.5001	5.016

Chapter 4.

Experiment and discussion

In this chapter, experiment process for 5 types of film structure will be studied. After measurement of the experiment data, proximity effect parameters were extracted with the double Gaussian model. The extracted parameters of proximity effect and GDS (graphic data system) file of designed patterns were inputted to PROXECCO, the proximity effect correction tool which is running at Sun work station, to generate proximity effect corrected file for Leica E-beam exposure system. The corrected exposure results were measured by SEM to check the capability of proximity effect correction.

4.1. Experiment process

4.1.1. Experiment equipments

1. Photo-resist coating and developing: Clean MK-8, TEL.
2. Exposure system：WePrint 200, Leica.
3. CD measurement: S6280, Hitachi.
4. Thickness measurement: n&k analyzer, model: NKT 1500.
5. Electronic balance: model: AG285, Mettler.
6. ESCA: model： Microlab 310F, VG Scientific.
7. EA: model: CHN-O-RAPID, Foss Heraeus.

4.1.2. Experiment process

The wafers were done film processing first. Then coating, exposure and developing processes were done. Measurement and inspection of the wafers followed. Proximity effect parameters were extracted from the measurement data. The procedure is depicted at Fig 4-1. Fig 4-2 shows the procedure for proximity effect correction check.

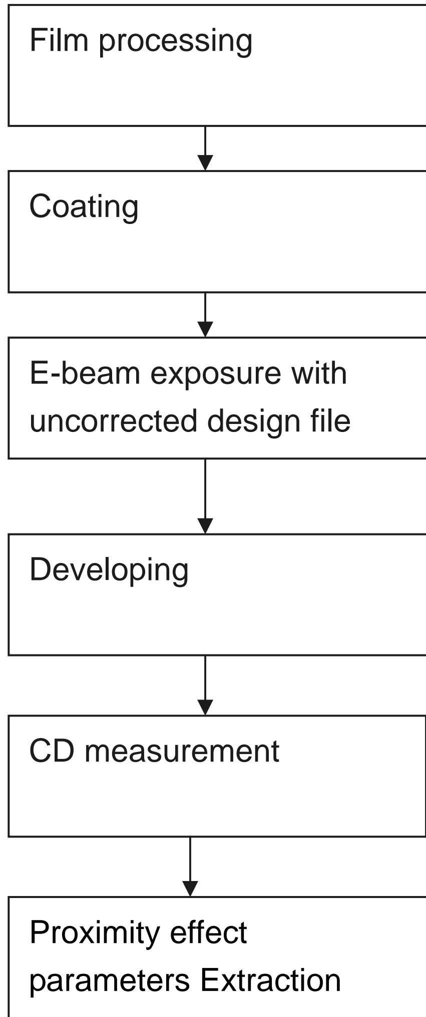

Fig 4-1 wafer process flow for proximity effect extraction with uncorrected design patterns.

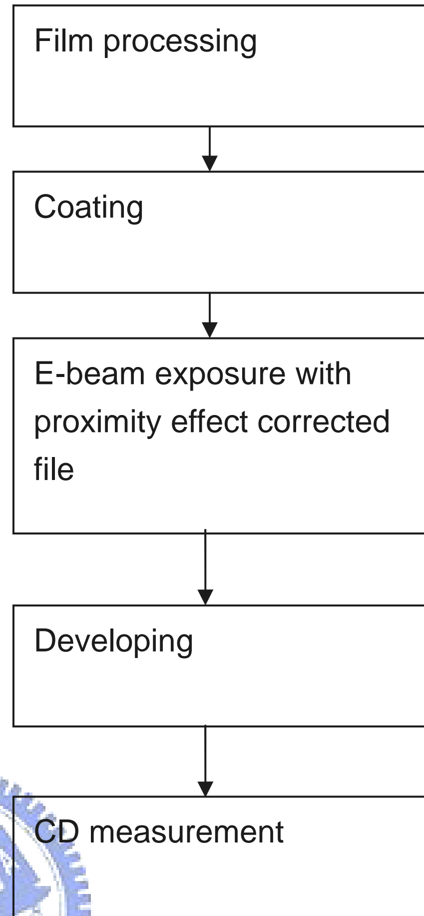

Fig 4-2 wafer process flow for proximity effect correction check with proximity effect correction patterns.

4.1.3. Clean Track coating

The wafers were primed with HMDS vapor to improve photoresist adhesion in AD-unit at TEL (Tokyo electric limited) Clean track first. After HMDS priming, the wafers were cooled by temperature control cool plate. After cooling, they were spin-coated with NEB-A2 photo-resist at coating module by dipping photoresist manually. Soft bake followed to evaporate most solvent at 110°C for 2 minutes.

4.1.4. E-beam exposure

The designed patterns were exposed by Leica WePrint-200.The exposure dosage were spanned from 1.1 to 8.0 uC/cm^2 with 0.1 uC/cm^2 step, 8.2 to 9.0 with 0.2 uC/cm^2 step, 9.5 to 15 with 0.5 uC/cm^2 step, and 16 to 20 with 1.0 uC/cm^2 step.

Leica WePrint-200 is a variable shape beam system. There are two diaphragms in the e-beam path. Each aperture has at least 4 square holes [31]. As the E-beam emit from the e-gun, the first deflection lens system will select one square of the first diaphragm for e-beam to pass. Then the second deflection lens system will select one square of the second diaphragm to pass and decide how much overlap with the input beam from the first diaphragm. A non-rotated hole could be combined with a rotated one to produce triangular shapes [31].

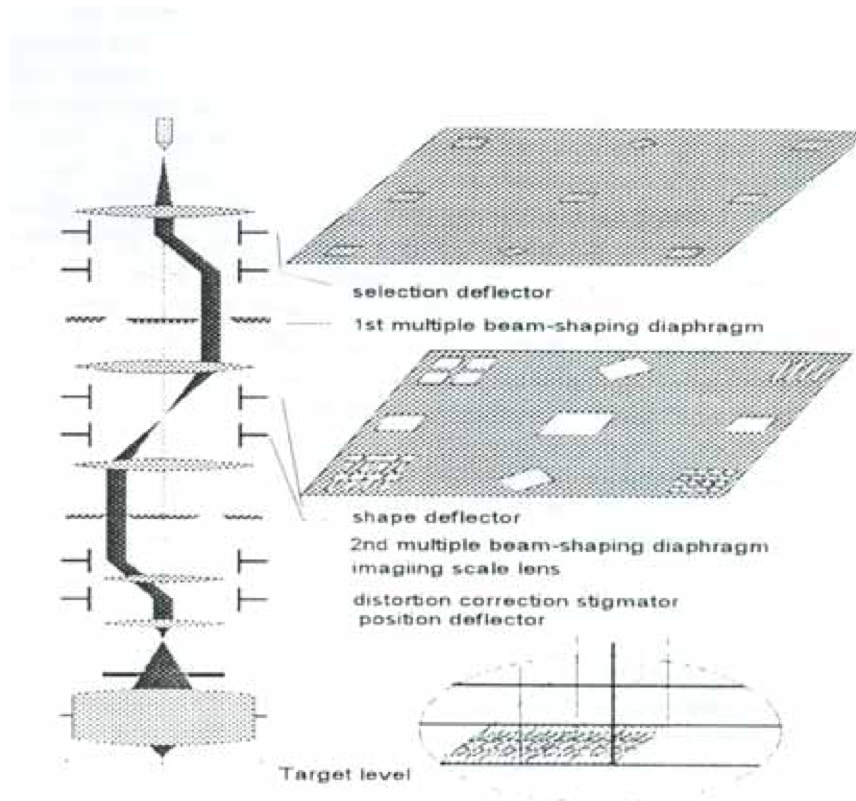

Fig 4-3 schematic drawing of beam path of Leica WePint 200 [31].

The maximum of the exposed area is 4x4 μm square. The smallest exposed square is 20x20 nm square. The stage use continuous moving method, write-on-the-fly technology. The scanning mode is vector scanning method. All of the above features improve the throughput of the system.

4.1.5. Clean Track developing

The exposed wafers were processed with PEB (post exposure bake) at 105°C for 2 minutes .Then they were developed with AD-10 developer at develop module. Finally, hard bake process at 110°C for 2 minutes dried the wafers and solidified the photo resist patterns at dehydration hot plate.

4.1.6. CD measurement

All of the wafers were measured and inspected by in-line SEM, Hitachi S6280. The maximum power of the SEM is 150K X. The accelerated voltage for the measurement is 700 V. The current is from 8.0 to 10.0μA. The system uses secondary electrons as signal source. Linear approximation algorithm for CD measurement was used through the experiment.

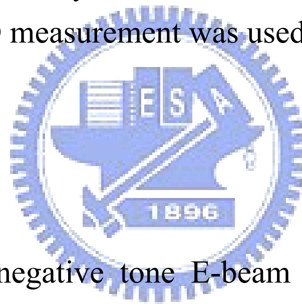

4.2. Test patterns

For the experiment, we used negative tone E-beam resist. Isolated lines, dense lines and trenches are common semiconductor circuit layout. Isolated dots and dense dots have two dimensional symmetries and thus are usually used for test patterns. So these 5 types of patterns of different sizes were used to evaluate proximity effect. The test patterns were drawn at Fig 4-4.

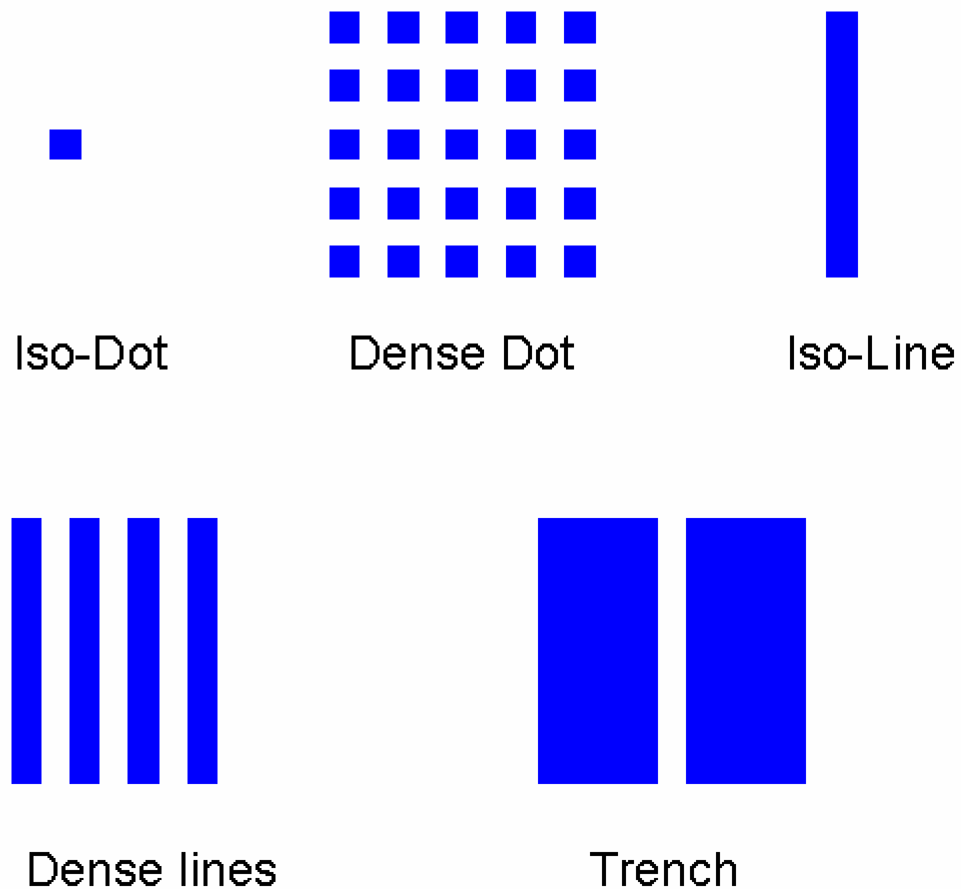

Fig 4-4 schematic drawing of designed patterns to extract proximity effect parameters and to check proximity effect correction result.

For dense lines, there are 5 duty ratios, 2/3,1/2,1/2.5,1/3 and 1/4. For Isolated-line, Dense line and Dense dot, 22 sizes of dimensions (40nm, 60nm, 80nm, 100nm, 120nm, 140nm, 160nm, 180, 200nm, 220nm, 240nm, 260nm, 280nm, 300nm, 350nm, 400nm, 500nm, 600nm, 800nm, 1μm, 2μm, 4μm) were designed. For Isolated-dot, 128 μm square was added. For trench type, all dimensions were times by 10 except the largest trench patterns. Thus the dimensions are from 400 nm to 20 μm.

The exposure area for all patterns except the largest isolated dots is 30X30 μm^2. The exposure area for the largest isolated dots is 128X128 μm^2.

4.3. Fitting algorithm

Proximity effect parameters were extracted with the double Gaussian model. The energy profile was obtained by convolution of equation (2.1), the double Gaussian functions of point

exposure, with the surface of test patterns as

$$E(x,y) = dose \cdot \iint_S f(x-x', y-y')dx'dy', \tag{4.1}$$

where x and y are the coordinate for the point for calculation. x' and y' are the coordinate of exposed pattern and are used for convolution with the exposure intensity distribution equation. For example, a rectangular pattern of CDx width and CDy height exposed by a dosage d, the energy profile can be obtained as the following equations.

$$\begin{aligned}
E(x,y) &= d \cdot \int_{-\frac{CD_y}{2}}^{\frac{CD_y}{2}} \int_{-\frac{CD_x}{2}}^{\frac{CD_x}{2}} f(x-x', y-y')dx'dy' \\
&= \frac{d}{\pi(1+\eta)}\left[\frac{1}{\alpha^2}\int_{-\frac{CD_y}{2}}^{\frac{CD_y}{2}} \int_{-\frac{CD_x}{2}}^{\frac{CD_x}{2}} e^{\frac{(x-x')^2+(y-y')^2}{\alpha^2}} dx'dy' + \frac{\eta_E}{\beta^2}\int_{-\frac{CD_y}{2}}^{\frac{CD_y}{2}} \int_{-\frac{CD_x}{2}}^{\frac{CD_x}{2}} e^{\frac{(x-x')^2+(y-y')^2}{\beta^2}} dx'dy'\right] \\
&= \frac{d}{4\pi(1+\eta)}\left\{\begin{aligned} &[erf(\frac{x+CD_x/2}{\alpha})-erf(\frac{x-CD_x/2}{\alpha})][erf(\frac{y+CD_y/2}{\alpha})-erf(\frac{y-CD_y/2}{\alpha})] \\ &+[erf(\frac{x+CD_x/2}{\beta})-erf(\frac{x-CD_x/2}{\beta})][erf(\frac{y+CD_y/2}{\beta})-erf(\frac{y-CD_y/2}{\beta})] \end{aligned}\right\}
\end{aligned} \tag{4.2}$$

Here constant threshold energy model was used to simulate the developed resist profile. Constant threshold model uses a constant threshold energy, Dth, for determination of the developed profile. For negative resist, the photoresist will be developed away if the deposited energy is less than the threshold energy and vice versa. We extracted the parameters Dth, α, β and η_E by minimized of CD error percentage. We also gave different weightings to lines patterns (isolated-lines and dense-lines). For the first method, the weightings of lines, isolated lines and dense lines are 2 and the others are 1. Because the isolated lines pattern are the most important feature for circuit, especially for transistor gate length. Dense lines patterns are also important to do high pattern density circuit, like SRAM. We will call this method Exp-Ext-W2 hereafter. For the other method, the weightings of wider lines (0.3~4 μm) are 10 and the other weightings are the same as the first method. It will minimize the error induced by measurement of patterns with small dimension. And we name the method Exp-Ext-W10.

4.4. Film structure

We used 6 inches silicon wafers. All wafers except silicon-substrate-only have one intermedium layer. The top of all wafers were coating with NEB-A2 photoresist. We used

negative tone E-Beam resist, NEB-A2, through the experiment. As for sub-100 nm need, we chose NEB-A2 to prevent PR collapse for sub-100 nm features. The photoresist thickness is 200 nm.

There are five types of exposed structure in this test. The simplest case of the exposed structure is coating the photoresist 200 nm film on 6 inches silicon substrate. It is the most often used one for test and monitor.

200 nm of copper film was deposited on the silicon wafers with ULVAC Sputter SBH-3308RDE of NDL. Then the wafers were coated with 200 nm photo-resist film before E-beam exposure.

300 nm of Tantalum film was deposited on the silicon wafers with ULVAC Sputter SBH-3308RDE of NDL. Then the wafers were coated with 200 nm photo-resist film before E-beam exposure.

200 nm of silicon dioxide film was grown at horizontal furnace (ASM/LB45 Furnace system) of NDL. Then the wafers were coated with 200 nm photo-resist film before E-beam exposure.

200 nm of silicon nitride film was deposited at horizontal furnace (ASM/LB45 Furnace system) of NDL. Then the wafers were coated with 200 nm photo-resist film before E-beam exposure.

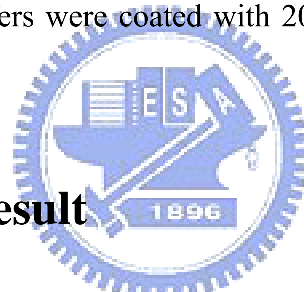

4.5. Experiment result

The developed wafers were inspected by optical microscope after development in track. The clear exposure dosage was identified by 128 μm square which has the least dosage and has photo-resist residue. The dimensions of exposed patterns with exposure of 2 and 3 times clear exposure dosage were measured. Then the proximity effect parameters were extracted by non-linear least fitting of the measured data. The proximity effect parameters extracted from different methods for different structures of film will be listed and compared.

4.5.1. Proximity effect parameters of Exp-Ext-W2 method

Proximity effect parameters of Exp-Ext-W2 were extracted from the experiment measurement data and are listed at Table 4-1. The forward scattering ranges of different structures are small and almost the same. It is consistent that the forward scattering depends on the top photo-resist thickness, the characteristic of the photo-resist and the E-beam accelerating voltage. And it does not depend on the film structure. The backward scattering range of Ta is very different from other films. The density and atomic number of Ta is large compared to other films, so the

backscattering effect is serious from the Ta Film and the range is small compared to other films. The energy reflection ratio of Ta is the largest as expected.

Table 4-1 Proximity effect parameters extracted from the measurement data with Exp-Ext-W2 weightings.

	Dth	α (nm)	β (μm)	η_E
Si	2.5	69	9.944	0.658
Cu	3	61	12.887	0.822
Oxide	2.8	58	6.381	0.698
SN	2.9	61	7.599	0.645
Ta	2.2	51	1.285	1.013

4.5.2. Proximity effect parameters of Exp-Fit-W10 method

The proximity effect parameters of Exp-Ext-W10 are also obtained and listed at Table 4-2. The forward scattering ranges also show the same behavior as the previous method. The backward scattering ranges of all films except Ta show a little larger than the previous method. The energy reflection ratio shows consistent with the previous method.

Table 4-2 Proximity effect parameters extracted from the measurement data with Exp-Ext-W10 weightings.

	Dth	α (nm)	β (μm)	η_E
Si	2.4	67	14.415	0.815
Cu	3.1	58	12.214	0.808
Oxide	2.84	58	7.33	0.677
SN	3	56	9.14	0.668
Ta	2.3	51	1.147	0.999

4.5.3. Proximity effect parameters comparison of different method

The energy reflection ratios of backscattering to the forward scattering will be compared first. Ta film got the highest backscattering effect for both the empirical method and Mont Carlo method due to large atomic number and the highest density. Except silicon-substrate process, the energy reflection ratios from two empirical methods are about the same. The reflection ratios of all films, except Ta, are larger than the Monte Carlo method. For nitride and oxide layer, this phenomenon may come from charging effect due to low conductivity of the films. The measurement data of copper process were not enough to do correct extraction due to serious pattern lifting.

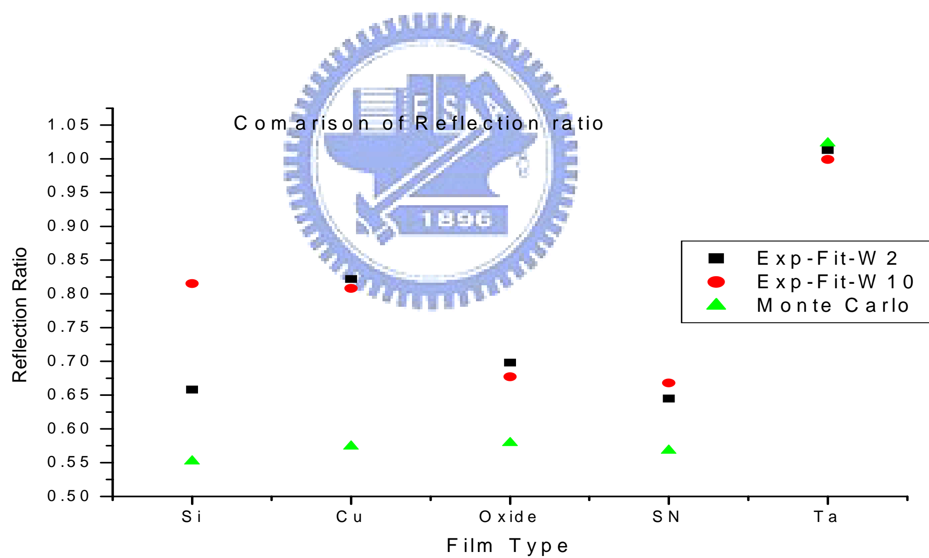

Fig 4-5 Comparison chart of backscattering energy to forward scattering energy ratio for 5 types of substrates.

The backscattering distribution chart is shown at Fig 4-6. For Ta film, backscattering ranges are very similar for all three methods and they got the smallest backscattering ranges as expected. The backscattering ranges of oxide and nitride shows very similar for all three methods. Except silicon process, the backscattering range shows consistent between two extraction methods of different weightings. The differences of backscattering range of copper maybe come from not enough data for extracting because all of the small patterns on copper film lift away due to poor adhesion. The fitting will be difficult to get the correct parameters.

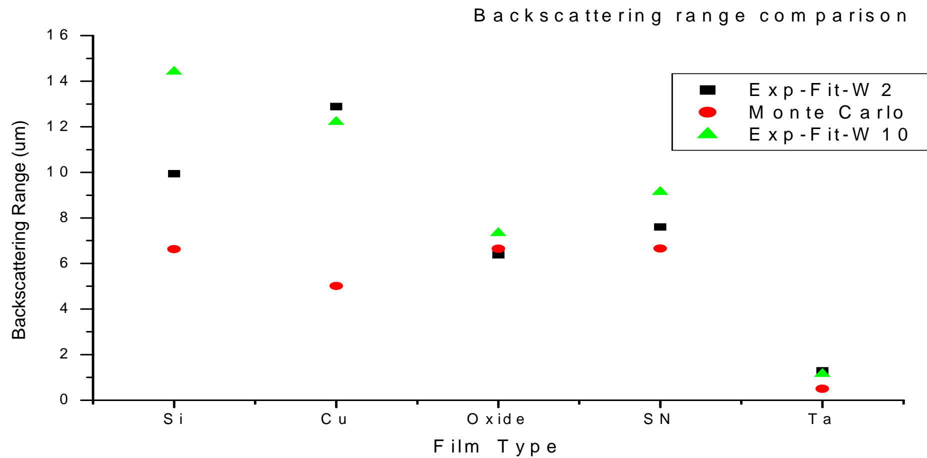

Fig 4-6 Comparison chart of backscattered range for 5 types of substrates.

From simulation, the forward scattering range, α, is about 1 nm. From experiment fitting, it is about 50 nm. It is due to the diffusion effect of the photoresist, NEB. The diffuse effect could be check by the cross link density method [32]. The silicon-substrate got large difference between the 2 extracting methods of different weight. It may come from the measurement error of some data. Thus the 2 extracting methods may confirm the correctness of the experiment. If it exist large difference, there must be some error during the experiment.

4.5.4. Proximity correction result of Si substrate

Measurement result of the silicon process will be shown from Fig 4-7 to Fig 4-11. It is clear that the proximity effect was corrected adequately from the ADI CD comparison chart of trenches, Fig 4-7. All of the 3 sets of proximity effect parameters work well. For isolated lines patterns, the uncorrected ones show good performance because the backscattering effect is very little for small dimension isolated lines. 80 nm isolated lines of design were printed successfully for all fitting parameters. From Fig 4-9, the deviation of dense lines patterns' CD was reduced a lot. But it still can not meet requirement, within 10 percent. All of the deviation shows that the patterns were over exposed due to strong proximity effect. From Fig 4-10, it also shows that the dense dots were over exposed, too. From Fig 4-11, the isolated dots were under exposed. All corrected patterns show the similar results. Fig 4-12 to Fig 4-14 show the SEM images of isolated line with various proximity effect correction methods.

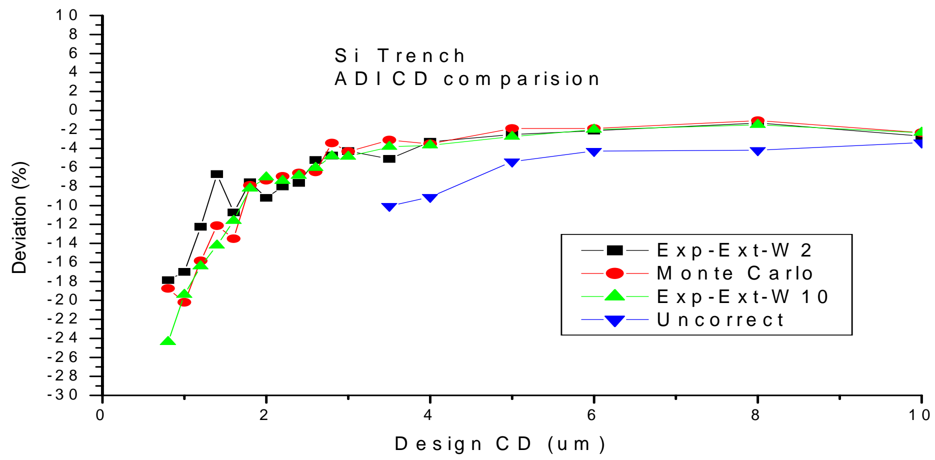

Fig 4-7 ADI CD comparison of silicon trench for proximity effect correction parameters from empirical and Monte Carlo methods.

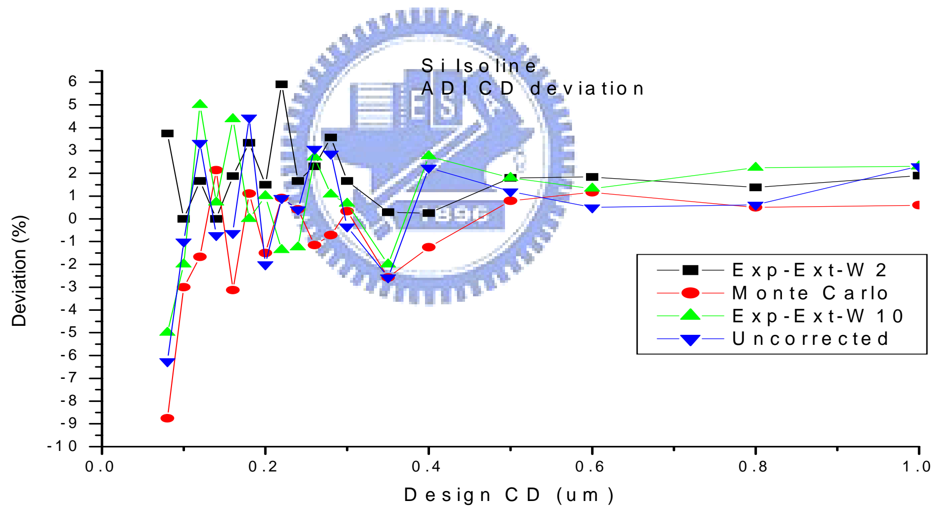

Fig 4-8 ADI CD comparison of silicon Isolated lines for proximity effect correction parameters from empirical and Monte Carlo methods.

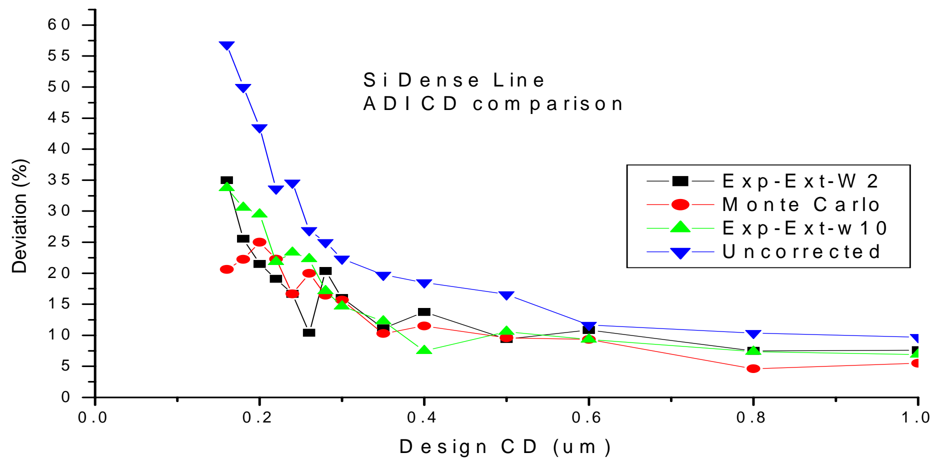

Fig 4-9 ADI CD comparison of silicon dense lines for proximity effect correction parameters from empirical and Monte Carlo methods.

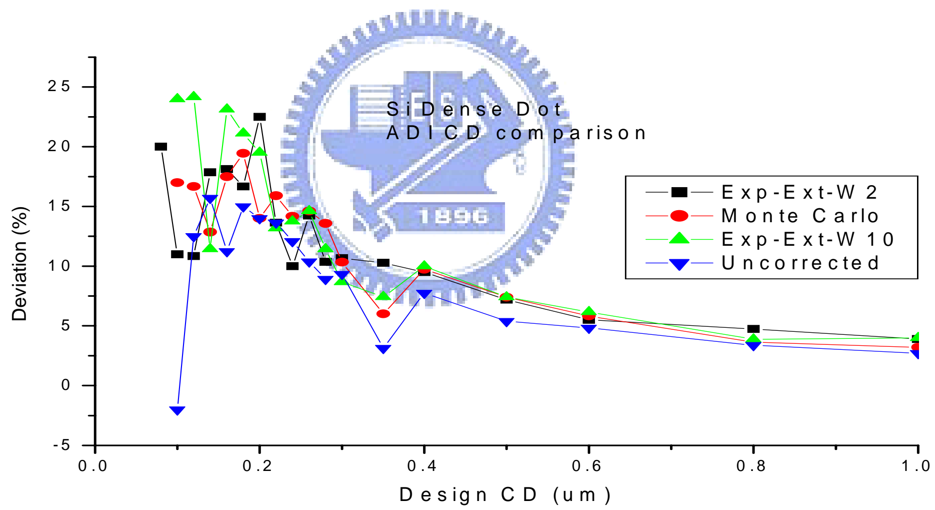

Fig 4-10 ADI CD comparison of silicon dense dots for proximity effect correction parameters from empirical and Monte Carlo methods.

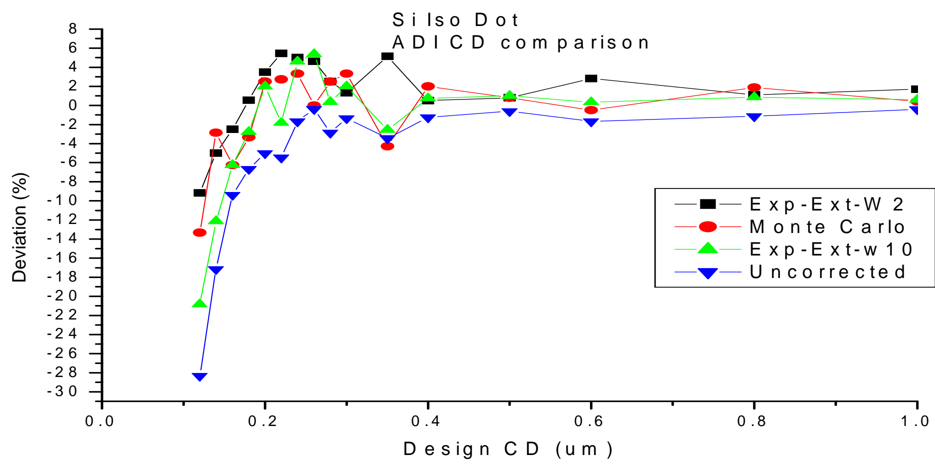

Fig 4-11 ADI CD comparison of silicon isolated dots for proximity effect correction parameters from empirical and Monte Carlo methods.

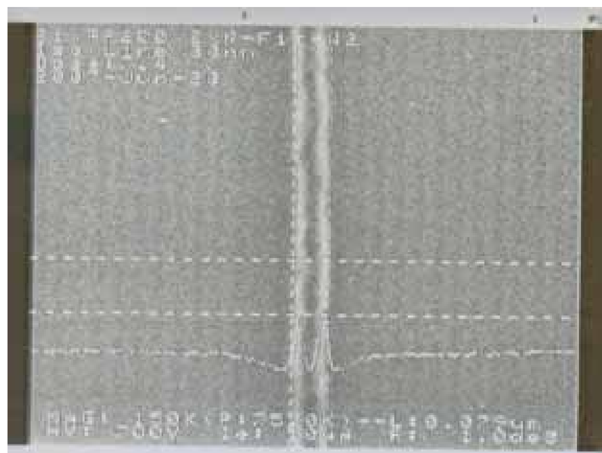

Fig 4-12 Proximity correction result of 80 nm silicon isolated line with Exp-Ext-W2 method. The design CD is 80nm. The measured CD is 79nm.

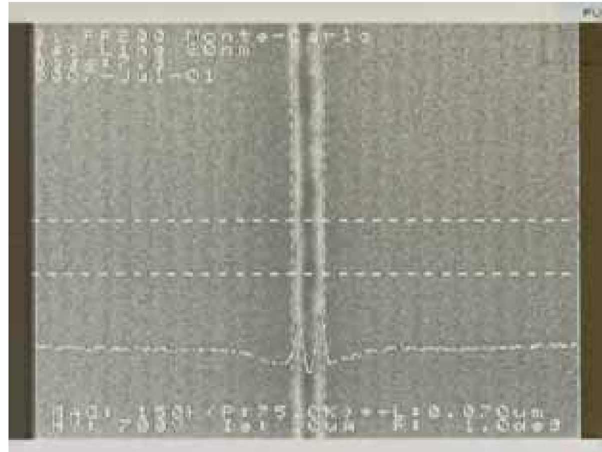

Fig 4-13 Proximity correction result of 80 nm silicon isolated line with Monte Carlo method. The design CD is 80nm. The measured CD is 70nm.

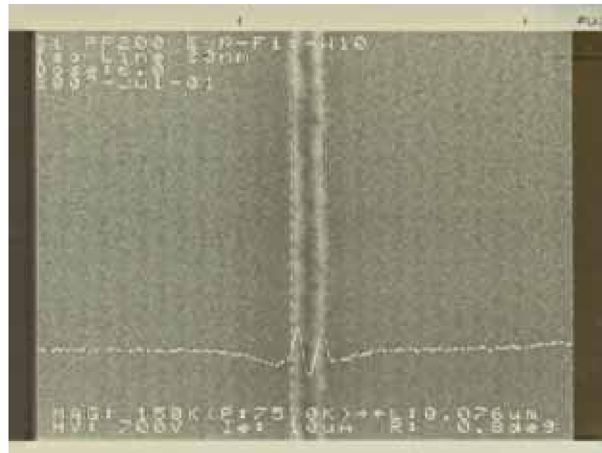

Fig 4-14 Proximity correction result of 80 nm silicon isolated line with Exp-Ext-W10 method. The design CD is 80nm. The measured CD is 76nm.

4.5.5. Proximity correction result of Nitride film

Measurement result of the nitride process will be shown from Fig 4-15 to Fig 4-19. From Fig 4-15, it is clear that the proximity effect was corrected adequately. All of the 3 sets of proximity effect parameters work well. From Fig 4-16, 80 nm isolated lines were printed successfully for all corrected methods. From Fig 4-17, the deviation of dense lines patterns' CD was reduced not much. All of the deviation shows that the patterns were over exposed. From Fig 4-18, Exp-Ext-W10 and Monte Carlo method work well. From Fig 4-19, the isolated dots were under exposed for small features. Most of the corrected patterns show better results. Fig

4-20 to Fig 4-22 show the SEM images of isolated line with various proximity effect correction methods.

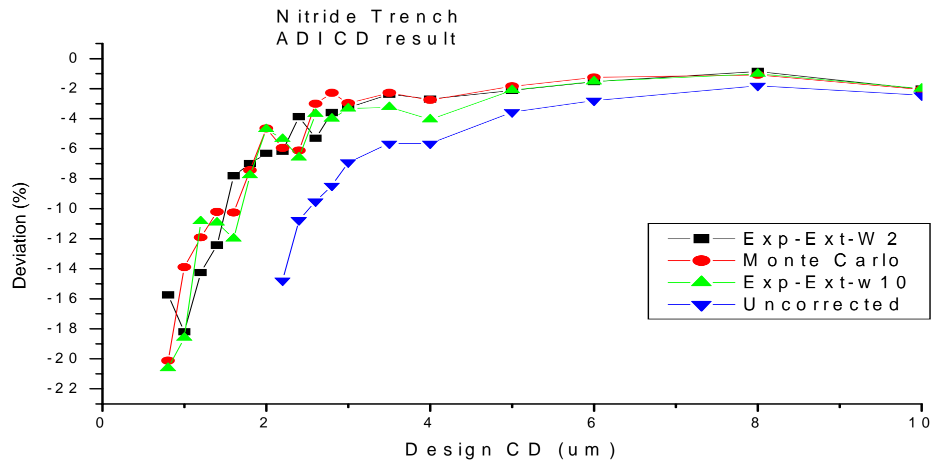

Fig 4-15 ADI CD comparison of nitride trench for proximity effect correction parameters from empirical and Monte Carlo methods.

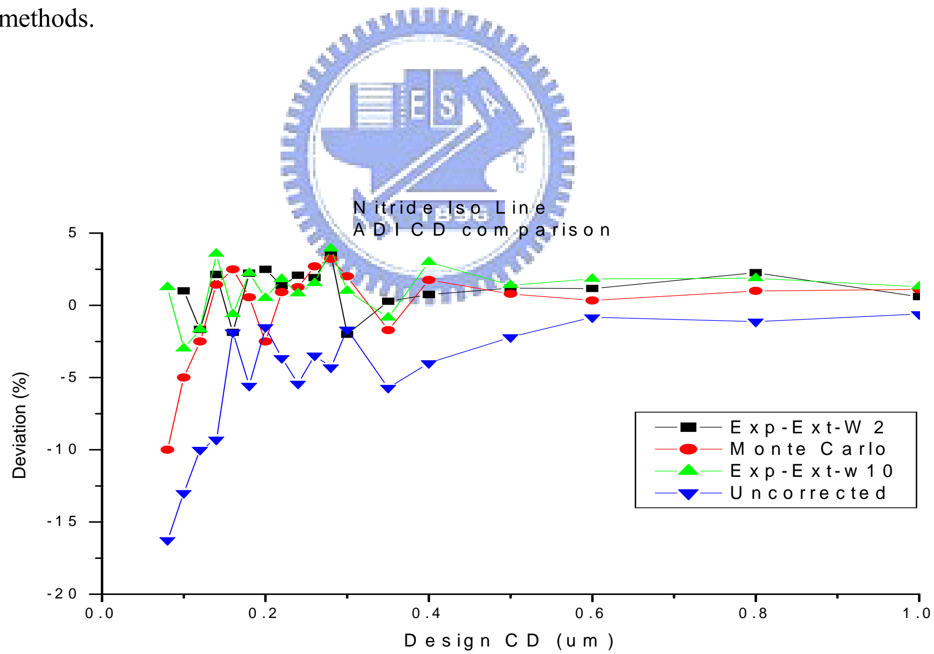

Fig 4-16 ADI CD comparison of nitride isolated lines for proximity effect correction parameters from empirical and Monte Carlo methods.

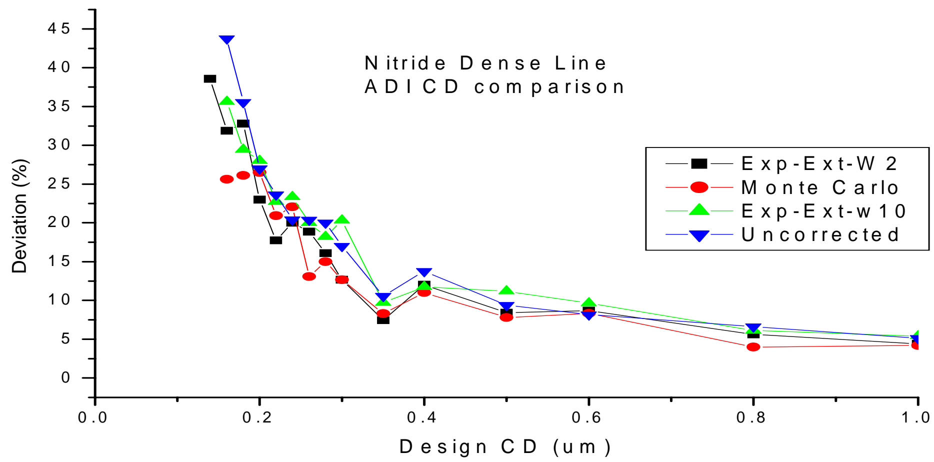

Fig 4-17 ADI CD comparison of nitride dense lines for proximity effect correction parameters from empirical and Monte Carlo methods.

.

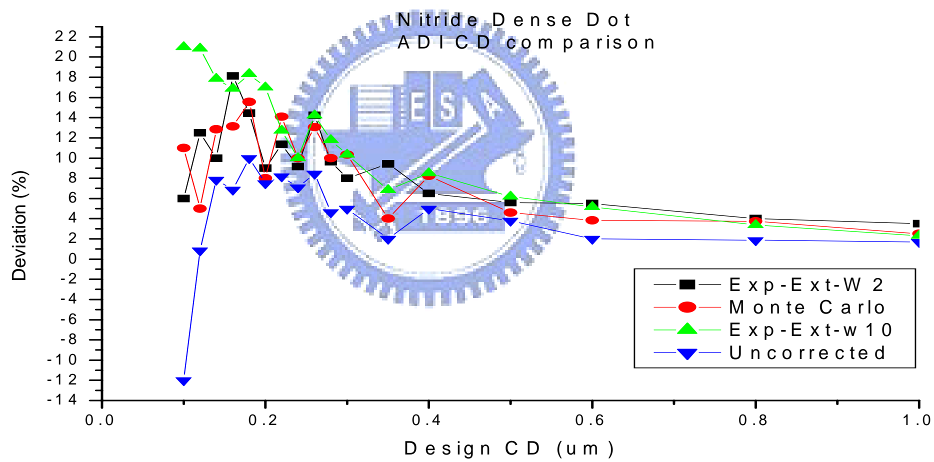

Fig 4-18 ADI CD comparison of nitride dense dots for proximity effect correction parameters from empirical and Monte Carlo methods.

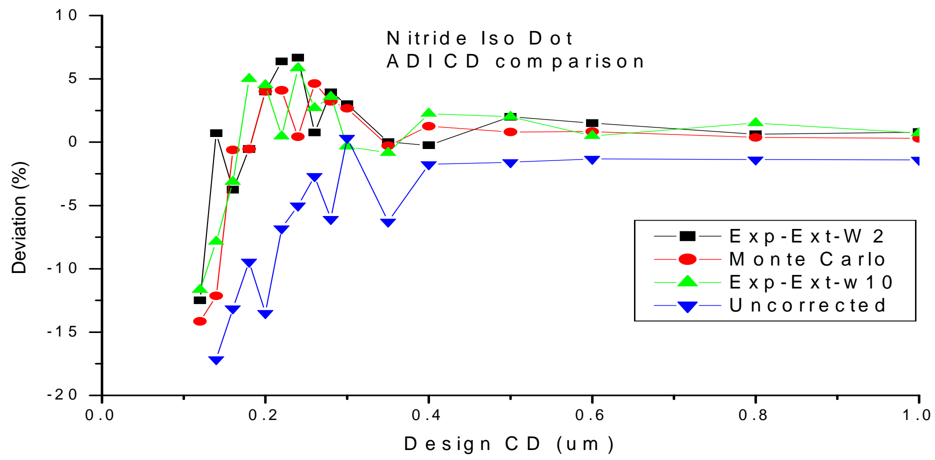

Fig 4-19 Nitride Isolated Dot ADI CD comparison for proximity effect correction parameters from empirical and Monte Carlo methods.

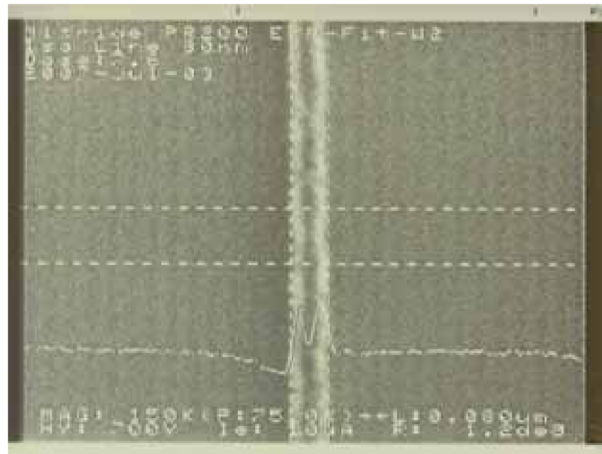

Fig 4-20 Proximity correction result of 80 nm nitride isolated line with Exp-Ext-W2 method. The design CD is 80nm. The measured CD is 80nm.

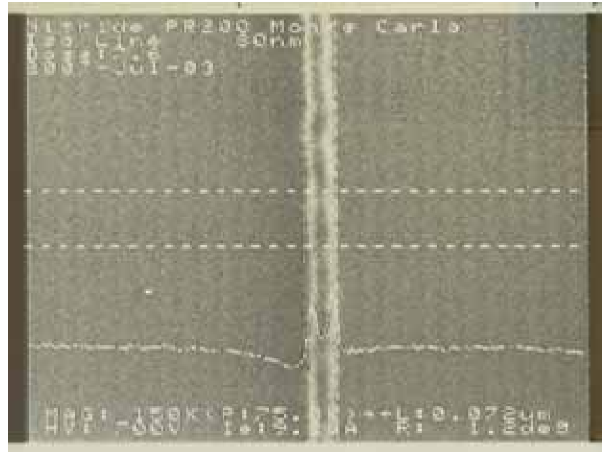

Fig 4-21 Proximity correction result of 80 nm nitride isolated line with Monte Carlo method. The design CD is 80nm. The measured CD is 72nm.

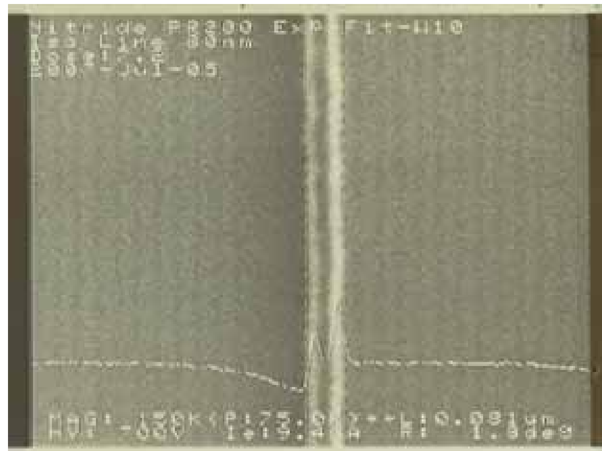

Fig 4-22 Proximity correction result of 80 nm nitride isolated line with Exp-Ext-W10 method. The design CD is 80nm. The measured CD is 81nm.

4.5.6. Proximity correction result of Wet-Oxide film

Measurement result of the wet-oxide process will be shown from Fig 4-23 to Fig 4-27. From Fig 4-23, it shows that the proximity effect was corrected adequately. All of the 3 sets of proximity effect parameters work well. 80 nm isolated lines were printed successfully for all corrected methods at next figure. From Fig 4-25, the deviation of dense lines patterns' CD was reduced a little. All of the deviation shows that the patterns were over exposed. From Fig 4-26, All of the corrected dense dot are over exposed. From Fig 4-27, the isolated dots were under exposed for small features. Most of the corrected patterns show better and consistent results.

Fig 4-28 to Fig 4-30 show the SEM images of isolated line with various proximity effect correction methods.

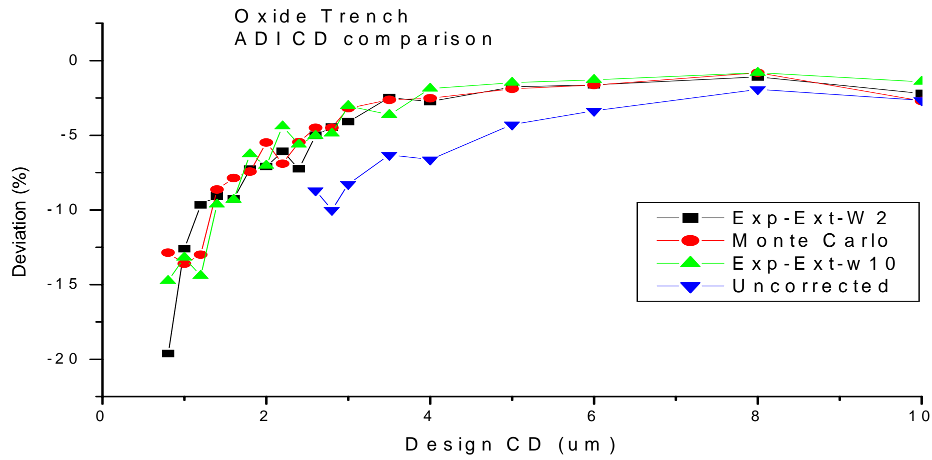

Fig 4-23 ADI CD comparison of wet oxide trench for proximity effect correction parameters from empirical and Monte Carlo methods.

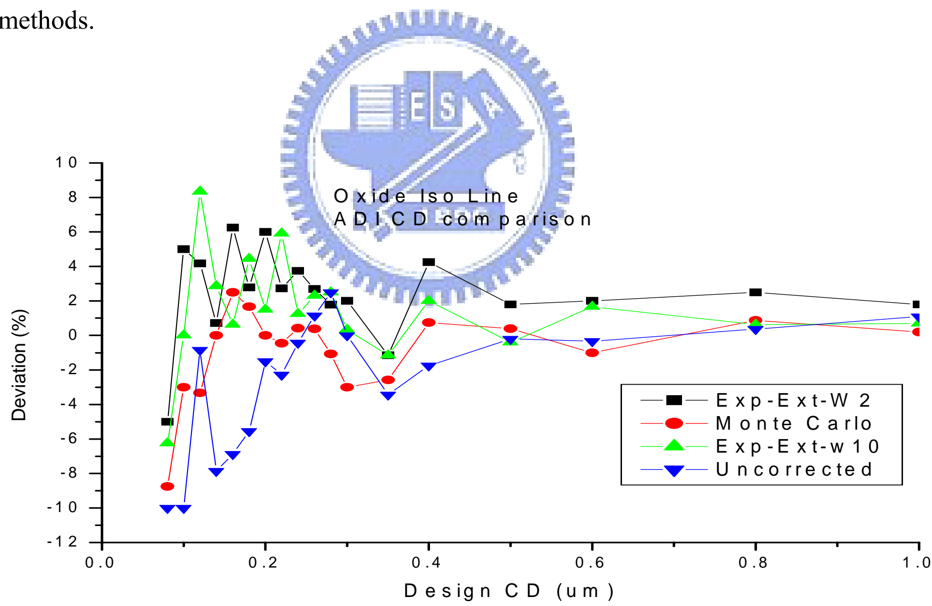

Fig 4-24 ADI CD comparison of wet oxide isolated lines for proximity effect correction parameters from empirical and Monte Carlo methods.

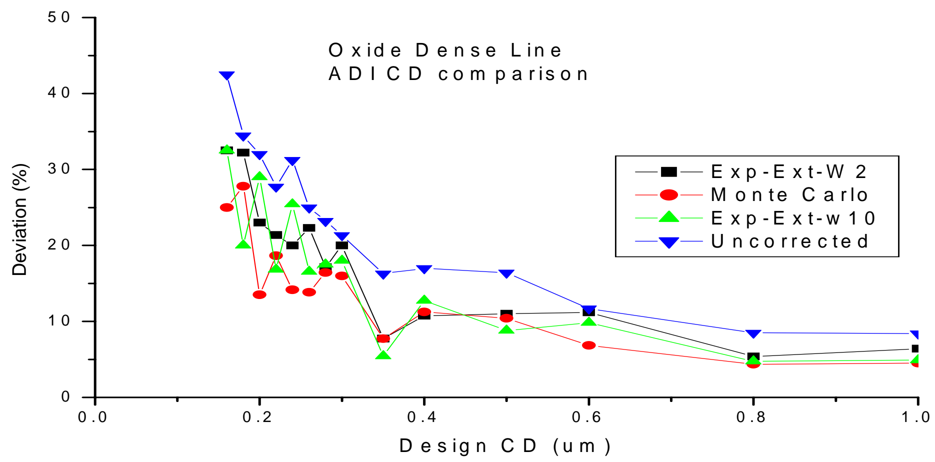

Fig 4-25 ADI CD comparison of wet oxide dense lines for proximity effect correction parameters from empirical and Monte Carlo methods.

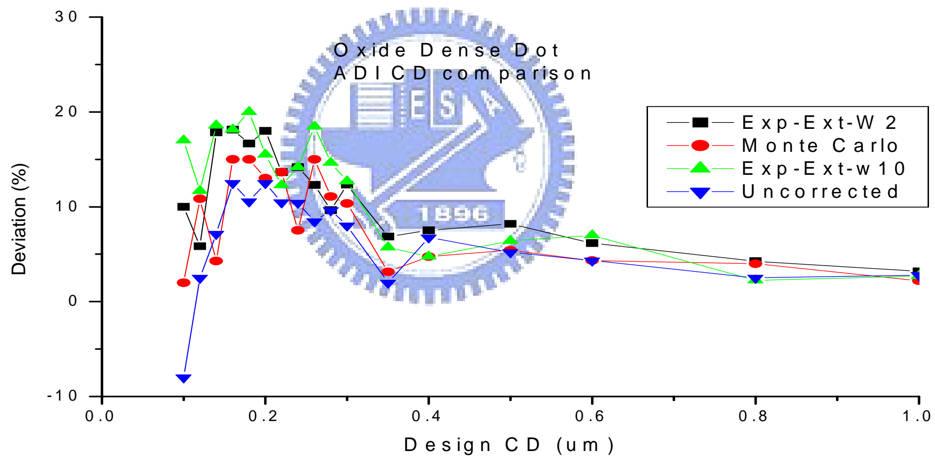

Fig 4-26 ADI CD comparison of wet oxide dense dots for proximity effect correction parameters from empirical and Monte Carlo methods.

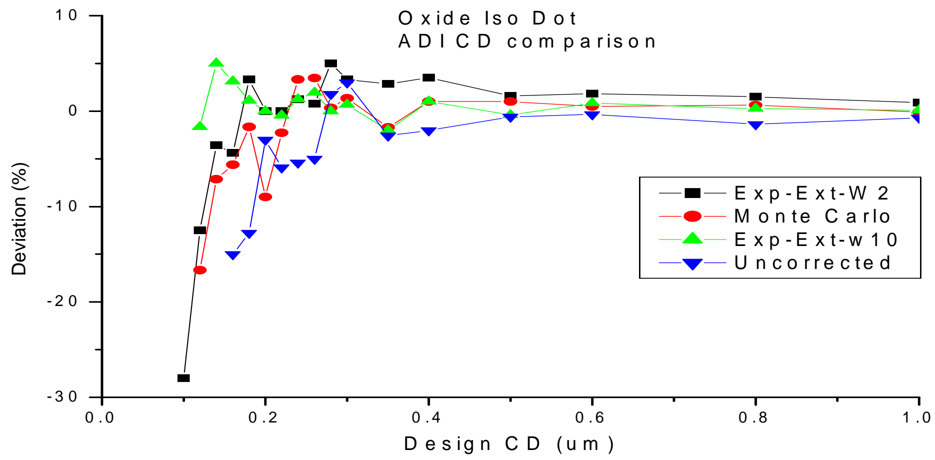

Fig 4-27 Wet Oxide Isolated Dot ADI CD comparison for proximity effect correction parameters from empirical and Monte Carlo methods.

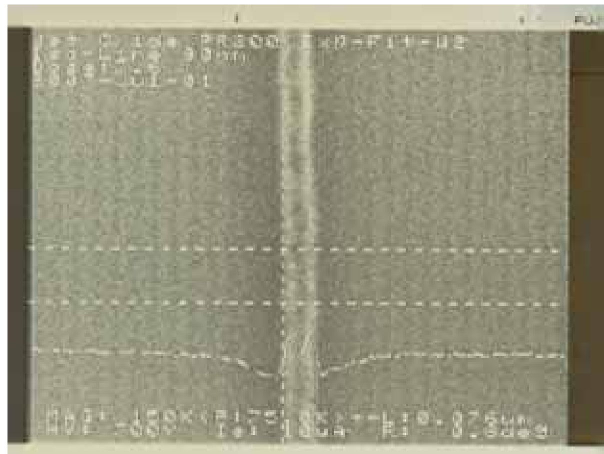

Fig 4-28 Proximity correction result of 80 nm wet oxide isolated line with Exp-Ext-W2 method. The design CD is 80nm. The measured CD is 76nm.

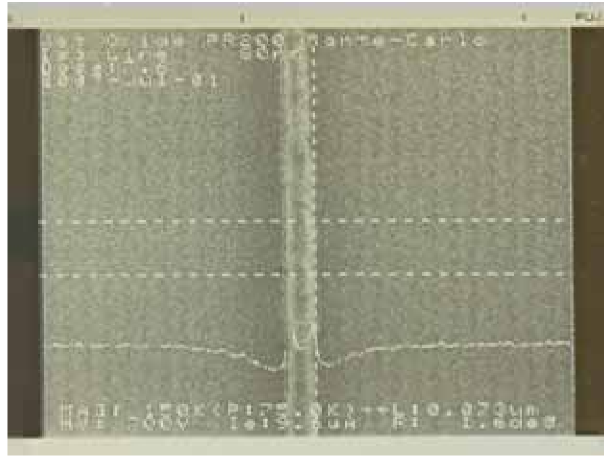

Fig 4-29 Proximity correction result of 80 nm wet oxide isolated line with Monte Carlo method. The design CD is 80nm. The measured CD is 73nm.

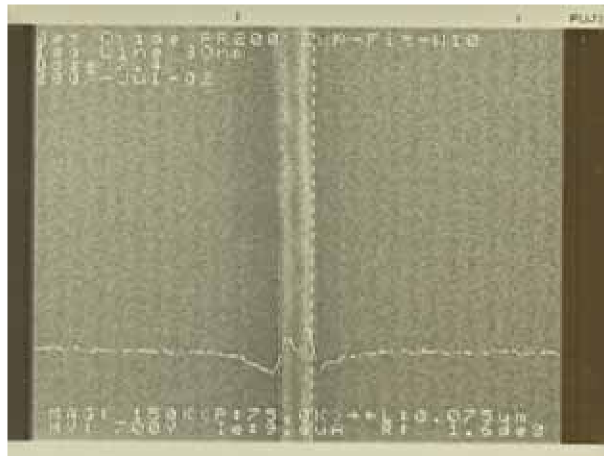

Fig 4-30 Proximity correction result of 80 nm wet oxide isolated line with Exp-Ext-W10 method. The design CD is 80nm. The measured CD is 75nm.

4.5.7. Proximity correction result of Ta film

Measurement result of the Ta process will be shown from Fig 4-31 to Fig 4-35. From Fig 4-31,it is clear that the proximity effect was corrected well. All of deviation the 3 compensation methods is less than 10 percent. Although the backward to forward energy ratio of Ta is the largest, the proximity effect of trench is not serious as other films due to small backscattering range. The backscattering range is only about 1 μm for Ta film. If the distance between adjacent patterns is larger than 1 μm, the proximity effect will not be serious. 80 nm isolated lines were a little under exposed at next figure. From Fig 4-33, all of the deviation shows that

the patterns were over exposed. The data of proximity effect parameters of Monte Carlo show the worst results because the wrong selected energy. We can see from all figures that it got over exposed. From Fig 4-34, The proximity effect parameters extracted from experiment methods work well. From Fig 4-35, the isolated dots were under exposed for small features. Most of the corrected patterns show better and consistent results. Fig 4-36 to Fig 4-38 show the SEM images of isolated line with various proximity effect correction methods.

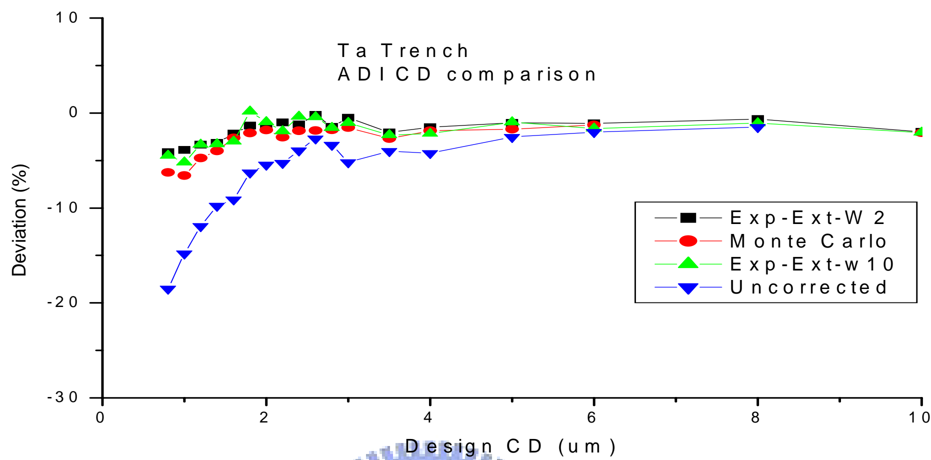

Fig 4-31 ADI CD comparison of Ta trench for proximity effect correction parameters from empirical and Monte Carlo methods.

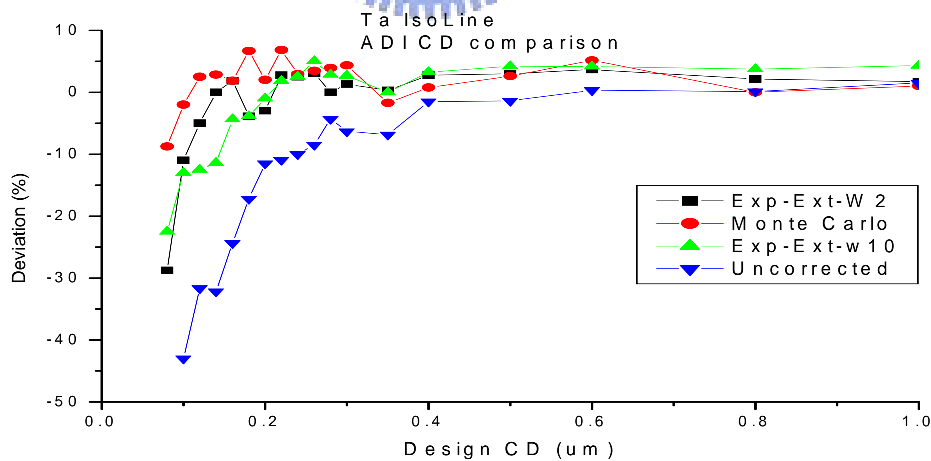

Fig 4-32 ADI CD comparison of Ta isolated lines for proximity effect correction parameters from empirical and Monte Carlo methods.

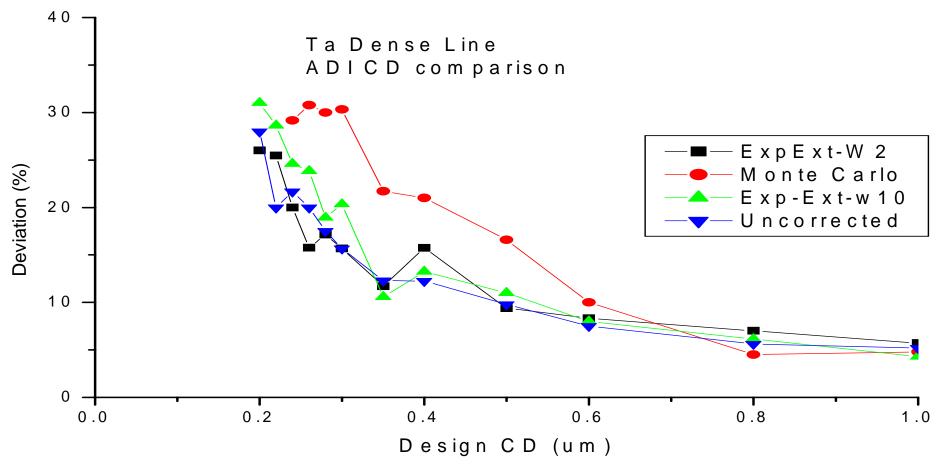

Fig 4-33 ADI CD comparison of Ta dense lines for proximity effect correction parameters from empirical and Monte Carlo methods.

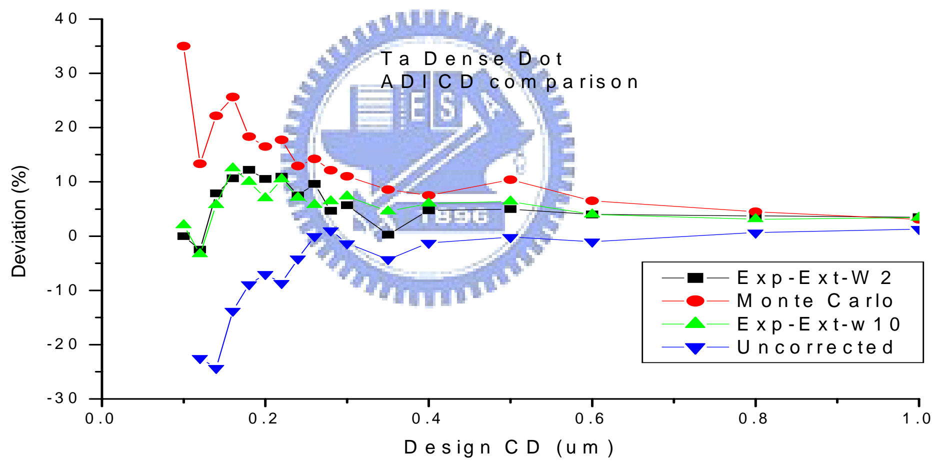

Fig 4-34 ADI CD comparison of Ta dense dots for proximity effect correction parameters from empirical and Monte Carlo methods.

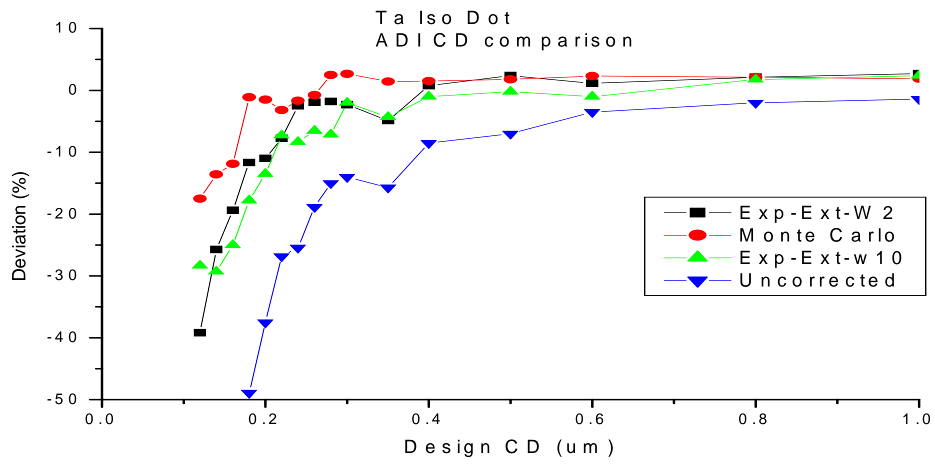

Fig 4-35 ADI CD comparison of Ta isolated dots for proximity effect correction parameters from empirical and Monte Carlo methods.

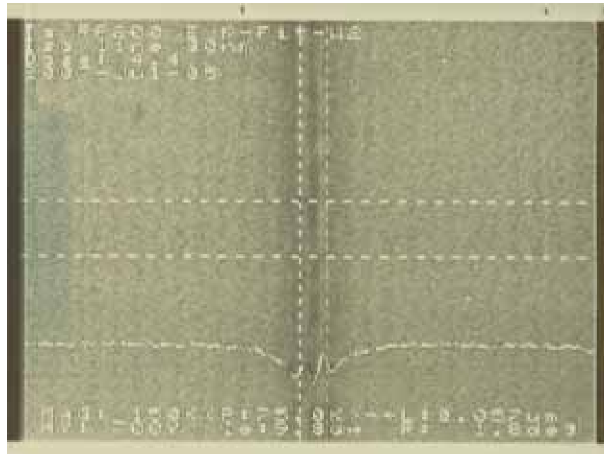

Fig 4-36 Proximity correction result of 80 nm Ta isolated line with Exp-Ext-W2 method. The design CD is 80nm. The measured CD is 57nm.

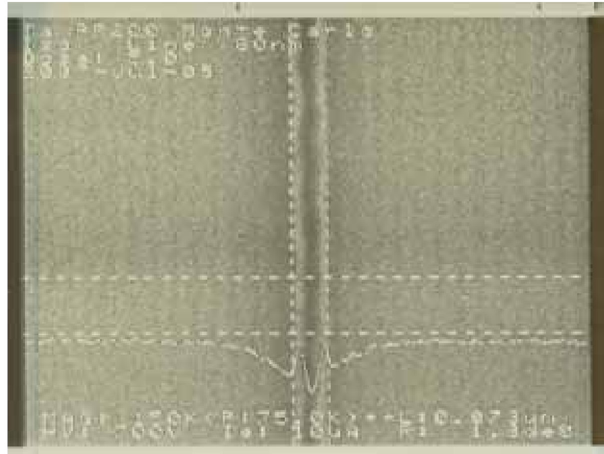

Fig 4-37 Proximity correction result of 80 nm Ta isolated line with Monte Carlo method. The design CD is 80nm. The measured CD is 73nm.

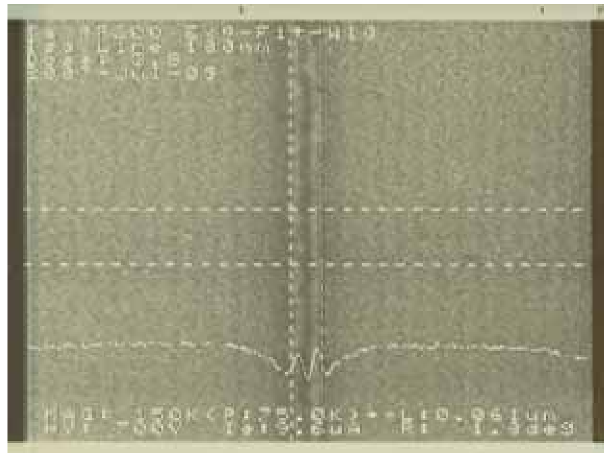

Fig 4-38 Proximity correction result of 80 nm Ta isolated line with Exp-Ext-W10 method. The design CD is 80nm. The measured CD is 61nm.

4.5.8. Proximity correction result of Copper film

Measurement result of the copper process will be shown from Fig 4-39 to Fig 4-43. From Fig 4-39,it is clear that the proximity effect was corrected well. All of the 3 sets of proximity effect parameters work adequately. From Fig 4-40, all of the small features, less than 200 nm, can't be measured due to serious photoresist lifting problem. From Fig 4-41, all of the deviation shows that the patterns were over exposed. The deviation trend charts of corrected and uncorrected patterns are almost the same. From Fig 4-42, The proximity effect parameters extracted from experiment methods are a little over exposed. From Fig 4-43, the proximity

effect parameters extracted from the experiment methods work well. Most of the corrected patterns show better and consistent results. Fig 4-44 to Fig 4-46 show the SEM images of isolated line with various proximity effect correction methods. The small dimension patterns were all lifted away due to poor photoresist adhesion.

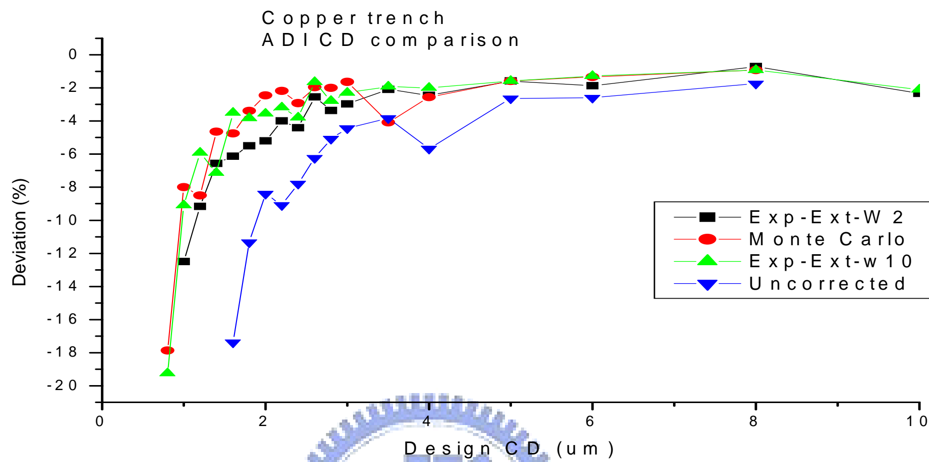

Fig 4-39 ADI CD comparison of copper trench for proximity effect correction parameters from empirical and Monte Carlo methods.

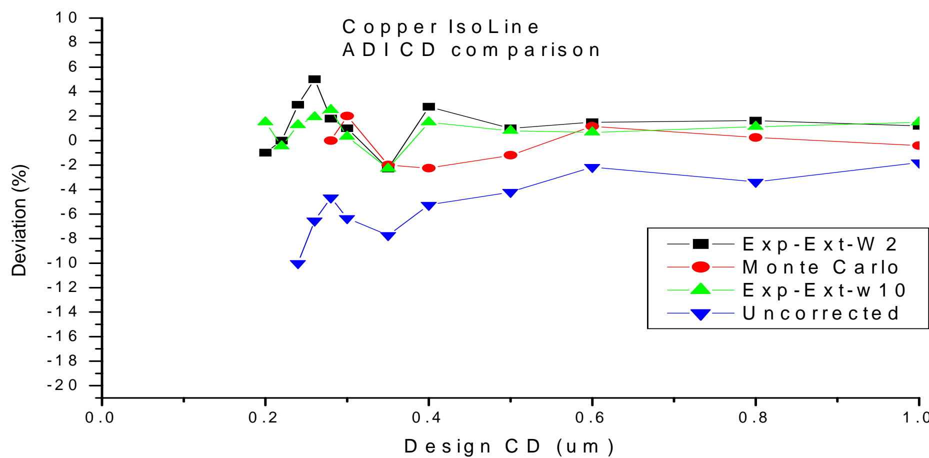

Fig 4-40 ADI CD comparison of copper isolated lines for proximity effect correction parameters from empirical and Monte Carlo methods.

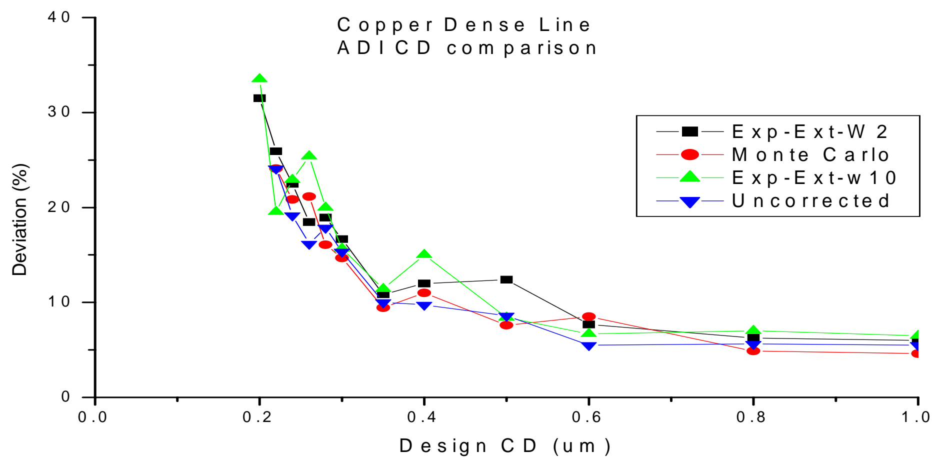

Fig 4-41 ADI CD comparison of copper dense lines for proximity effect correction parameters from empirical and Monte Carlo methods.

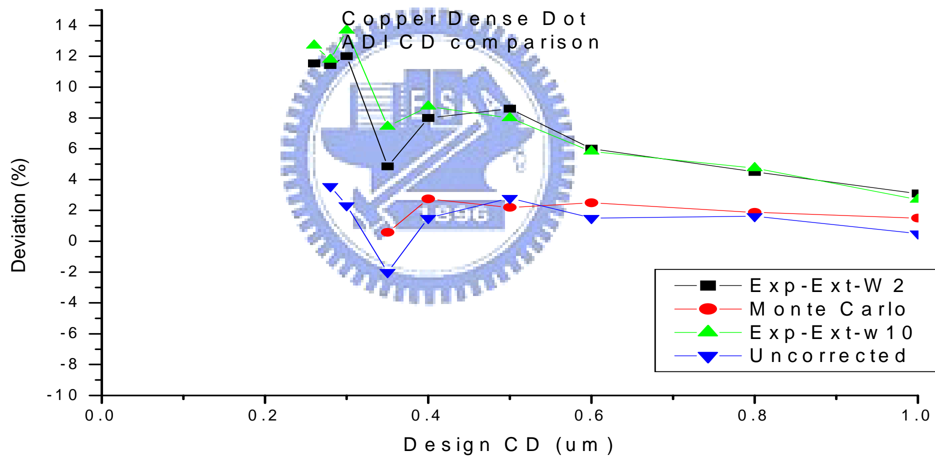

Fig 4-42 ADI CD comparison of copper dense dots for proximity effect correction parameters from empirical and Monte Carlo methods.

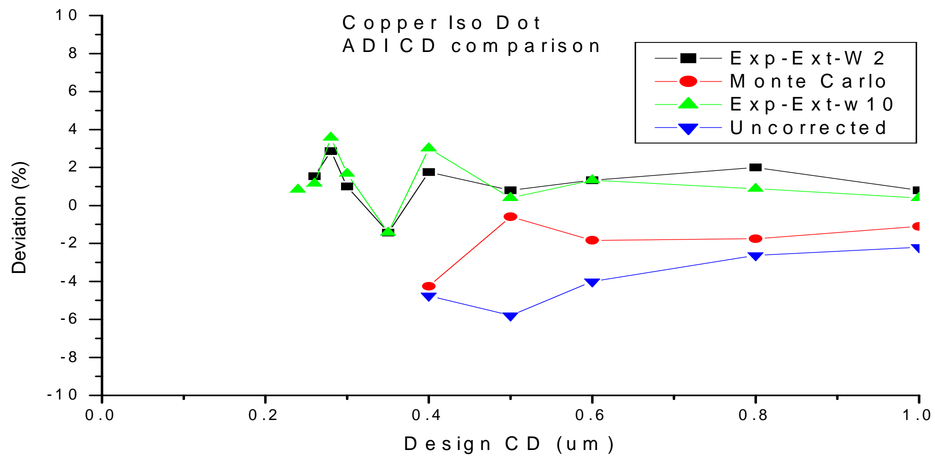

Fig 4-43 ADI CD comparison of copper isolated dots for proximity effect correction parameters from empirical and Monte Carlo methods.

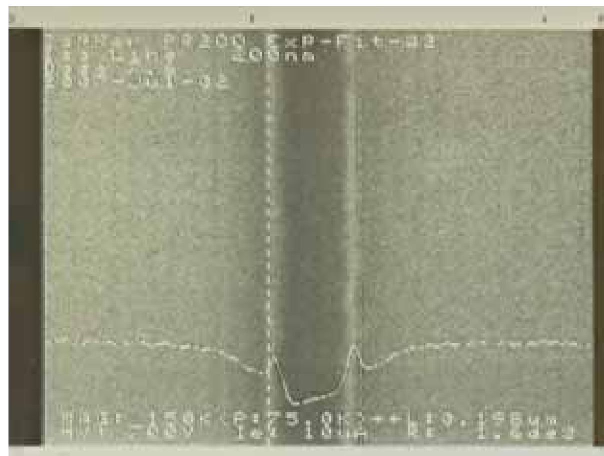

Fig 4-44 Proximity correction result of 200 nm Cu isolated line with Exp-Ext-W2 method. The design CD is 200nm. The measured CD is 198nm.

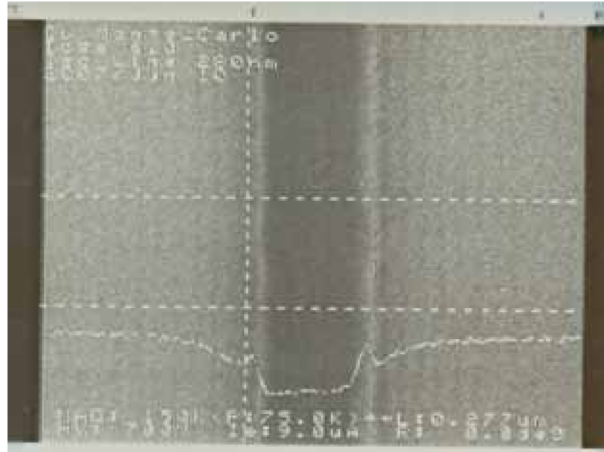

Fig 4-45 Proximity correction result of 280 nm Cu isolated line with Monte Carlo method. The design CD is 280nm. The measured CD is 277nm.

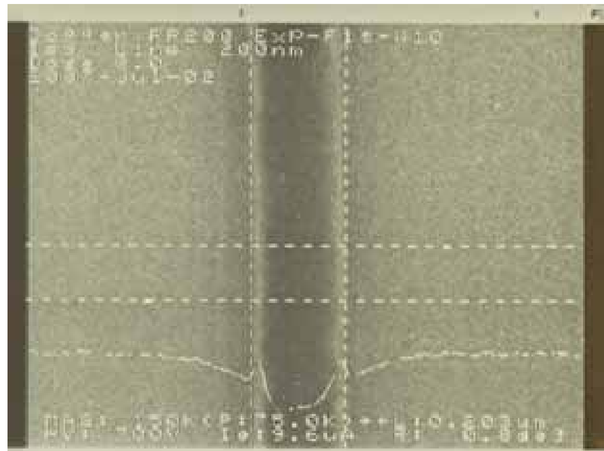

Fig 4-46 Proximity correction result of 200 nm Cu isolated line with Exp-Ext-W10 method. The design CD is 200nm. The measured CD is 203nm.

4.6. Discussion

Originally the measured dimension error of trench pattern is the largest due to large area exposure. From ADI CD comparison chart of trench patterns, Fig 4-7,Fig 4-15,Fig 4-23,Fig 4-31 and Fig 4-39, the deviation induced by proximity effect is greatly reduced after proximity correction. All of the proposed proximity effect parameters improve the performance of E-beam trench print capability.

For isolated lines, the features are the most important for MOS gates pattern. From ADI CD comparison chart, Fig 4-8,Fig 4-16 ,Fig 4-24 , Fig 4-32 and Fig 4-40, CD error induced by

proximity effect is also reduced after proximity correction. Sub-100 nm features were printed for all proximity correction exposed wafers except copper film. The poor photo-resist adhesion of copper film makes small pattern feature lifting seriously. The lifting of 260 nm isolated line of copper process was shown at Fig 4-47.

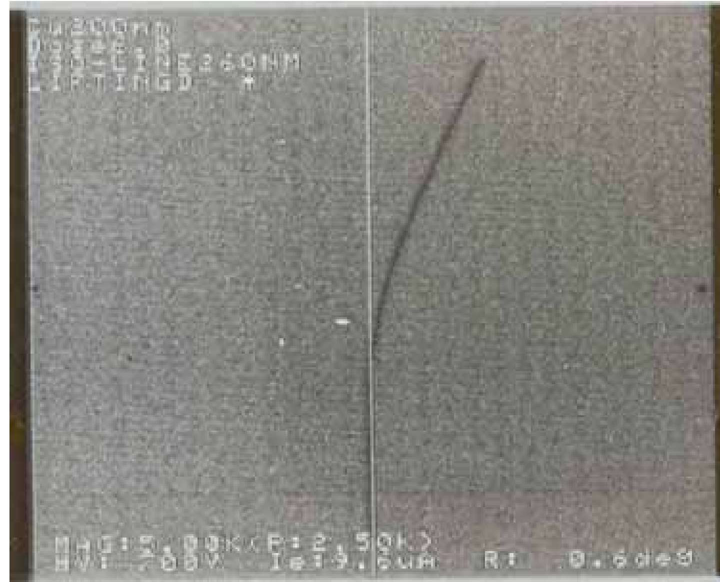

Fig 4-47 PR lifting of isolated line of 260 nm on copper film.

For dense lines, a little improvement was seen. But the proximity effect correction is not good enough. This is probably due to the fact that the exposure distribution does not accurately fit a double Gaussian distribution [12]. To better correct the proximity effect, Triple Gaussian proximity correction should be developed [12]. And lower backscattered coefficient could be obtained by using higher accelerating voltage, such as 100KV. And the backscattering range will be large. Thus the proximity effect could be alleviated by averaging effect. On the other way, low accelerating voltage (1~ 2 KV) systems were also used to do nanolithography. To prevent the proximity effect, a thick buffer layer was used under the photo-resist coating. The advantage of this process is that no proximity effect correction is needed [33].

For isolated dots patterns, the measured CDs of small dots (<150 nm) are smaller than the designed CD. This is due to the acid diffusion effect of the photoresist. The photo-resist, NEB, is a chemically amplified resist. The acid will diffuse during post exposure bake. The diffuse phenomenon effect could be check by cross link density [32]. The cross link density of NEB-A4 of 100 nm isolated line of the process is shown at Fig 4-48. The X coordinate is the print bias of the exposed pattern, and the cross link density is normalized to 1 for zero bias. For Fig 4-48, we could see that cross link density of 50 nm bias is about 0.6, so the exposure is the reciprocal of 0.6 and it is about 1.67 times of zero bias exposure. The diffusion phenomena could be check by the slope of cross link density of isolated lines.

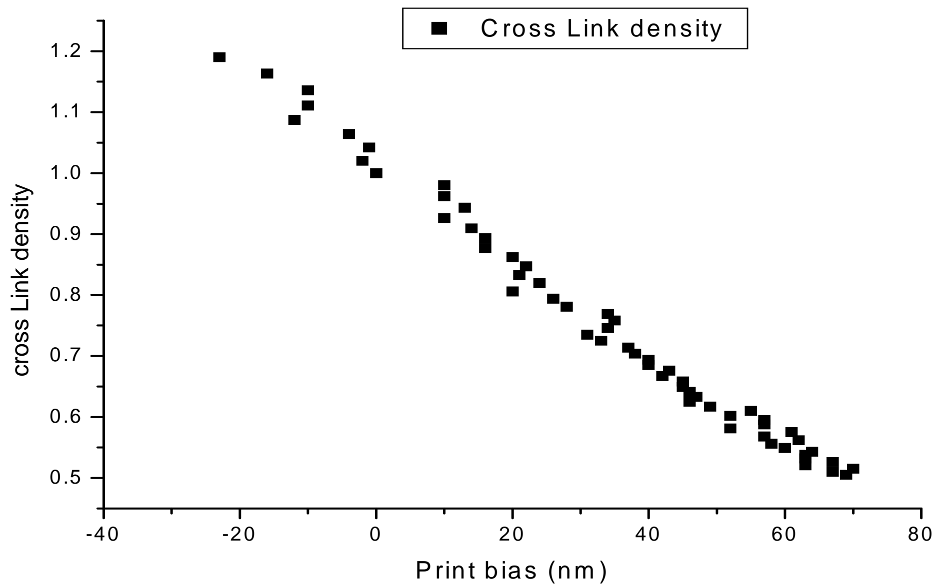

Fig 4-48 cross link density chart of 100 nm isolated line of NEB-A4 photoresist.

For dense dots, the proximity is not so serious. 100 nm dots could be printed both for corrected or non-corrected exposure methods. This is due to the counteraction result of diffusion effect and backscattering effect. The diffuse effect tends to reduce the exposure intensity of the pattern while the backscattering effect tends to increase the exposure intensity from adjacent patterns. 100 nm dense dots patterns could be obtained both for corrected and uncorrected exposure.

Chapter 5.

Conclusion and future work

Experimental fitting methods and Monte Carlo simulation method were developed to derive the proximity effects parameters. The parameters derived here can be combined with design patterns to obtain modified exposure data by PROXECCO. The proximity effects will be alleviated.

For Isolated-lines, 80 nm features were successfully exposed at Leica We-Print 200 after the proximity correction for all processes except copper's. For small features of copper process, the poor photo-resist adhesion made photo-resist patterns lift.

From the result of proximity effect parameters, the forward and backward scattering ranges and the energy ratio between backward and forward scattering from experiment fittings are larger than those from Monte Carlo method. This is due to diffusion effect of chemically amplified photo-resist.

The Monte Carlo simulation can make a quick solution for proximity correction. The result shows comparable with experiment fitting. It can serve for most experiment need.

In the future, wafers with different material film, such as high k, will be developed and tested. And wafers of multiple layer films, like ONO (Oxide-Nitride-Oxide) structure, will be developed and tested. The resist profile simulator and post exposure effect of chemically amplified resist will be developed.

Reference

1. Harry J. Levinson, Principles of Lithography, 2006.
2. ITRS 2005 edition, http://www.itrs.net/Links/2005ITRS/Home2005.htm
3. K.C.A. Smith and C.W. Oatley, "The scanning electron microscope and its fields of application," Br. J. Appl. Phys., Vol.6, 391-399, 1955.
4. T. Djenizian and P. Schmuki, "Electron beam lithographic techniques and electrochemical reactions for micro-and nanostructuring of surfaces under extreme conditions," J Electroceram, 9-14, 2006.
5. E. Webber and R. Moore, "Variable spot-shaped *e*-beam lithographic tool," Journal of Vacuum Science and Technology, 1780-1782, November 1979.
6. A. Yamada and H. Yasuda, "MCC system with CP," 2005 International Microprocesses and Nanotechnology Conference, 25-28 oct., 236-237, 2005.
7. http://www.mapperlithography.com/
8. C. Brandstttter, H. Loeschner, G. Stengl, G. Lammer, H. Buschbeck, E. Platzgummer, H. J. Doring, T. Elster and O. Fortagne, "Projection maskless lithography," Proc. SPIE 5374, 601-609, 2004.
9. H. C. Pfeiffer and W. Stickel, "Prevail - IBM's e-beam technology for next generation lithography," Future Fab Intl. Volume 12, 187-195, 2002.
10. T.H.P Chang, "Proximity effect in electron-beam lithography," J. Vac. Sci. Technol., Vol. 12 , No. 6, 1271-1275, Nov./Dec. 1975.
11. S.J. Wind Et al. "proximity correction for electron beam lithography using a three-Gaussian model of the electron energy distribution," J. Vac. Sci. Technol. B7, 1507-1512, 1989.
12. S. A. Rishton and D. P. Kern, "Point Exposure Distribution Measurements for Proximity Correction in electron Beam Lithography on a sub-100 nm Scale," J.Vac. Sci. Technol., 5(1), 135-141, 1987.
13. Sunao Aya et al., "Validity of Double and triple Gaussian Functions for Proximity Correction in X-ray Mask Writing," Jpn. J. Appl. Phys. Vol. 35, 1929-1936, 1996.
14. Hans Eisenmann, Thomas Waas and Hans Hartmann, "PROXECCO – Proximity effect correction by convolution," J. Vac. Sci. Technol., B 11(6), 2741-2745, Nov/Dec 1993.
15. L. Stevens et al., "Determination of the proximity parameters in electron beam lithography using Doughnut-Structure," Microelectronic Engineering, Vol. 54, 141-150, 1986.
16. http://www.aiss.de/sceleton/sceleton-index.html
17. Anja Rosenbusch et al., "SELID: a new 3D simulator for E-beam Lithography," SPIE Vol. 2884, 435-441, 1996.
18. N. Glezos and I. Raptis, "A fast electron beam lithography simulator based on the

Boltmann Transport Equation," IEEE transaction on computer-aided design of integrated circuits, Vol.15, No. 1, 92-102, Jan 1996.
19. M. Hintermaier, etc., "Proximity correction using computer aided proximity correction (CAPROX): Evaluation and application," J. Vac. Sci. Technol. B 9(6), 3043-3047, Nov/Dec 1991.
20. Mihir Parikh, "Self-Consistent proximity effect correction technique for resist exposure (SPECTRE)," J. Vac. Sci. Technol., 15 (3), 931-933, May/June 1978.
21. Geraint Owen and Paul Rissman, "Proximity effect correction for electron beam lithography by equalization of background dose," J. Appl. Phys. 54(6), 3573-3581, 1983.
22. Brian D. Cook and Soo-Young Lee, "PYRAMID - a Hierarchical, Rule-Based Approach Toward Proximity Effect Correction – Part II : correction," IEEE transaction on semiconductor manufacturing, Vol. 11, No. 1, 117-128, Feb. 1998.
23. R. J. Hawryluk, Andrew M. Hawryluk and Henry I. Smith, "Energy dissipation in a thin film by electron beam scattering," J. of applied physics 1, Vol. 45, No.6, 2551-2566, 1974.
24. Takao Utsumi, "Low-Energy E-beam Proximity Lithography (LEEPL): Is the Simplest the best?" Jpn. J. Appl. Phys. Vol. 38, Part 1, No. 12B, 7046-7051, Dec. 1999.
25. Ryuichi Shimizu and Ding Ze-Jun, "Monte Carlo modeling of electron-solid interactions," Rep. Prog. Phys., 487-531, 1992.
26. B. P. Nigam, M. K. Saunderson and Ta-You Wu, "Theory of multiple scattering: Second Born Approximation and Correction to Moliere's Work," Phys. Rev., 115, 491-502, 1959.
27. Toshiyuki Kijima and Yoshiaki Nakase, "Monte Carlo Calculations of the Behavior of 300 Kev Electrons from Accelerators," Radiation Measurements, VOL. 26, No. 2, 159-168, 1996.
28. http://www.random.org/
29. 蔡銘仁, "A study on Monte Carlo Simulation of Electron Beam Lithography," 國立交通大學電子工程研究所碩士論文, 2000.
30. Andrew R. Neureuther, David F. Kyser, Chiu H. Ting, "Electron-Beam resist edge profile simulation," IEEE transaction on electron devices, Vol. ED-26, NO. 4, 686-693, Apr. 1979.
31. O. Fortagne, P. Hahmann and Ch. Ehrlich, "WePrint 200 – The fast E-beam printer with high throughput," Microelectronic engineering 27, 151-154, 1995.
32. S. Landis et al., "Negative-tone chemically-amplified resist development for high resolution hybrid lithography," Microelectronic Engineering 73-74, 271-277, 2004.
33. K. D. Schock et al., "resist processes for low-energy electron-beam lithography," J. Vac. Technol. B 15(6), 2323-2326, 1997.

Vita

Chen-Hsiang Fang was born in Tainan on July 27, 1964. He received the B.S. degree in Mechanical Engineering in Chiao Tung University (NCTU) in 1986. He entered the College of Electrical and Computer Engineering of NCTU in February 2005. He received the M.S. degree from NCTU in August 2007.